1   **Title:**

2

3   **Comparative landscape of genetic dependencies in human and chimpanzee stem cells**

4

5   **Authors:**

6

7   Richard She[1,9], Tyler Fair[2,3,9], Nathan K. Schaefer[2,7], Reuben A. Saunders[1,4], Bryan J.
8   Pavlovic[2,7], Jonathan S. Weissman[1,5,6,8,*], Alex A. Pollen[2,7,10,*]

9

10 **Affiliations:**

11

12 [1]Whitehead Institute for Biomedical Research, Cambridge, MA, USA
13 [2]Eli and Edythe Broad Center of Regeneration Medicine and Stem Cell Research,
14 University of California, San Francisco, San Francisco, CA, USA.
15 [3]Biomedical Sciences Graduate Program, University of California, San Francisco, San
16 Francisco, CA, USA
17 [4]Department of Cellular and Molecular Pharmacology, University of California at San
18 Francisco, San Francisco, CA, USA.
19 [5]Department of Biology, Massachusetts Institute of Technology, Cambridge, MA, USA.
20 [6]Howard Hughes Medical Institute, Massachusetts Institute of Technology, Cambridge,
21 MA, USA.
22 [7]Department of Neurology, University of California, San Francisco, San Francisco, CA,
23 USA.
24 [8]David H. Koch Institute for Integrative Cancer Research, Massachusetts Institute
25 Technology, Cambridge 02142, MA
26 [9]These authors contributed equally: Richard She, Tyler Fair.
27 [10]Lead contact
28 *Correspondence: weissman@wi.mit.edu (J.S.W.), alex.pollen@ucsf.edu (A.A.P.)

29 **Abstract (150 word limit):**

30

31 Comparative studies of great apes provide a window into our evolutionary past, but the
32 extent and identity of cellular differences that emerged during hominin evolution remain
33 largely unexplored. We established a comparative loss-of-function approach to evaluate
34 whether changes in human cells alter requirements for essential genes. By performing
35 genome-wide CRISPR interference screens in human and chimpanzee pluripotent stem
36 cells, we identified 75 genes with species-specific effects on cellular proliferation. These
37 genes comprised coherent processes, including cell cycle progression and lysosomal
38 signaling, which we determined to be human-derived by comparison with orangutan cells.
39 Human-specific robustness to *CDK2* and *CCNE1* depletion persisted in neural progenitor
40 cells, providing support for the G1-phase length hypothesis as a potential evolutionary
41 mechanism in human brain expansion. Our findings demonstrate that evolutionary changes
42 in human cells can reshape the landscape of essential genes and establish a platform for
43 systematically uncovering latent cellular and molecular differences between species.

44

45

46

Introduction:

Comparative studies of humans and chimpanzees, our closest extant relatives, have long sought to define the evolutionary origins of unique human features. Within seven million years, humans evolved numerous specializations, from bipedalism to the threefold expansion of the cerebral cortex (Muller et al., 2017; Varki and Altheide, 2005). Many of these novel human traits emerge from changes in cell behavior during development. These changes in cell behavior may in turn create new requirements for existing genes and pathways that mediate evolutionary changes. However, we currently lack a framework for systematically identifying which molecular pathways play divergent roles in conserved developmental cell types.

Current approaches to studying the molecular basis of human evolution include reconstructing candidate mutations at specific loci in model organisms, but only a handful of mutations in non-coding regulatory regions and coding genes have been examined in detail. Among conserved non-coding elements with unexpected changes in the human lineage, specific loci have been linked to gene expression changes in distal limbs (Dutrow et al., 2022) increased sweat gland number (Aldea et al., 2021), and increased neural proliferation (Boyd et al., 2015). Among coding changes, two human-specific coding mutations in *FOXP2* have been proposed to contribute to human language capabilities based on functional studies in mouse models and human genetics (Enard et al., 2002; Lai et al., 2001), and three modern human-specific mutations in *KIF18A* and *KNL1* prolong metaphase and reduce segregation errors in neural progenitor cells (Mora-Bermúdez et al., 2022). In addition, recent duplications and subsequent modifications of *ARHGAP11B* and *NOTCH2NL* have been implicated in the expansion of the human cortex (Fiddes et al., 2018; Florio et al., 2016; Heide et al., 2020; Suzuki et al., 2018), supporting predictions that human-specific mutations may influence proliferation of neural progenitor cells during development (Kriegstein et al., 2006; Rakic, 1995). Nonetheless, connecting individual candidate mutations to evolved human traits remains challenging because the large majority of mutations are neutral or low effect size, analyses are low throughput, and we lack a detailed understanding of the divergence in cellular and developmental phenotypes that ultimately give rise to species differences.

In parallel, high-throughput genomics-based approaches have described gene regulatory changes that may contribute to species differences. Because ape primary tissue is largely inaccessible during early development, recent studies have employed stem cell derived models as an experimentally tractable system for comparative analyses of species differences during development. Thousands of cell-type specific gene expression differences have been identified in pluripotent stem cells (Gallego Romero et al., 2015; Marchetto et al., 2013), cardiomyocytes (Pavlovic et al., 2018), endoderm (Blake et al., 2018), neural crest (Prescott et al., 2015), and cortical neurons (Kanton et al., 2019; Marchetto et al., 2019; Pollen et al., 2019). However, these gene expression differences comprise a mixture of neutral changes, causal changes, and indirect downstream consequences and genes that mediate species differences may have conserved expression.

91 Therefore, it can be difficult to ascertain which molecular changes, among hundreds or
92 thousands, drive differences in cellular physiology.
93
94 The history of developmental genetics provides a rich template for linking the function of
95 individual genes to organismal phenotypes. Early mutagenesis screens in *Drosophila*
96 *melanogaster* identified genes critical for body axis patterning (Nüsslein-Volhard and
97 Wieschaus, 1980; Wieschaus and Nüsslein-Volhard, 2016). Many of these genes belonged
98 to highly conserved cell signaling pathways that also coordinate development in
99 vertebrates, such as Wnt (Miller, 2001; Peifer and Wieschaus, 1990), Hedgehog (Hooper
100 and Scott, 1989), and BMP (Costa et al., 1994). More recent efforts in organismal screening
101 involve several international consortia that have generated large collections of knockout
102 mice to investigate more complex vertebrate phenotypes (Dickinson et al., 2016; Hrabě de
103 Angelis et al., 2015; White et al., 2013). The success of these genetic approaches has
104 resulted in the functional annotation of many of the genes and regulatory networks that
105 guide mammalian development. Yet, although many core developmental principles are
106 conserved from fruit flies to mice to humans, these shared molecular functions do not
107 account for how our species evolved to be different.
108
109 To apply functional genomics approaches to questions of species divergence, we leveraged
110 recent advances in CRISPR-based technologies that have enabled genome-scale
111 perturbation screens across thousands of human cell lines (Gilbert et al., 2014; Sanjana et
112 al., 2014; Wang et al., 2014). These efforts have mapped landscapes of genetic
113 dependencies with an enrichment of essential genes in coherent pathways that typically
114 cluster by cell type of origin (Pacini et al., 2021; Tsherniak et al., 2017). Extending this
115 approach to studies of comparative evolution might reveal genes or cellular processes with
116 divergent functional roles in homologous cell types. Illuminating the extent and identity of
117 recently-evolved genetic dependencies would complement individual candidate gene
118 approaches, descriptive comparative genomics analyses, and single species loss-of-
119 function studies. However, whether genetic dependencies diverged in closely-related
120 hominin species and how this knowledge could reveal previously unappreciated
121 differences in cellular physiology remains unexplored.
122
123 To evaluate the extent of conservation and divergence in genetic dependencies between
124 human and chimpanzee, we established a comparative loss-of-function screening approach
125 in pluripotent stem cells (PSCs). PSCs are a model for the earliest stages of development,
126 capturing features of the inner cell mass of the blastocyst, including the capacity to
127 differentiate into all germ layers at a stage that precedes species differences in
128 developmental timing and cell type composition. The state of pluripotency is well
129 conserved between human and chimpanzee PSCs at the level of the transcriptome,
130 epigenome, and cell fate potential (Gallego Romero et al., 2015), and thus provides a
131 homologous cell type for species comparison. In addition PSCs have greater levels of open
132 chromatin and gene expression than somatic cells (Gaspar-Maia et al., 2011), enabling
133 large-scale study of gene function for genes later expressed in diverse cell types. As PSCs
134 are poised to self-renew or differentiate into all germ layers based on environmental cues,

4

135 we reasoned that changes in proliferation in PSCs could provide a sensitive measure for
136 species-specific responses to a wide range of genetic perturbations.
137
138 Performing genetic screens using an *in vitro* model confers several advantages that could
139 support isolation of molecular and cellular species differences. First, the ability to grow
140 large numbers of PSCs enables a pooled library approach with multiple redundant library
141 elements targeting each gene. Second, laboratory cell culture provides a well-defined and
142 highly controlled environment, which minimizes extrinsic sources of variation. Lastly, the
143 scalability of pooled screening allows for retesting of each cellular phenotype in PSCs
144 derived from multiple individuals of each species to account for individual variation within
145 a species. Thus, we harnessed the power of modern functional genomics to conduct
146 genome-wide CRISPR-interference (CRISPRi) screens in human and chimpanzee PSCs.
147 Despite high levels of conservation, our screens revealed that genetic dependencies can
148 diverge in remarkably short evolutionary time scales, that species differences are organized
149 into coherent pathways and protein complexes, and that human-specific changes have
150 evolved in gene networks promoting G1/S progression in PSCs and neural progenitor cells.
151 In addition to these specific insights, our study establishes a novel and broadly applicable
152 experimental approach for uncovering latent molecular differences between closely-related
153 species.
154
155 **Genome-wide CRISPRi screening in human and chimpanzee stem cells**
156
157 To enable comparative CRISPR-based genetic screening, we engineered CRISPRi
158 machinery (Gilbert et al., 2014) at the CLYBL safe harbor locus (Cerbini et al., 2015) in
159 two human and two chimpanzee pluripotent stem cell lines (Figure 1A). For the two human
160 representatives, we chose two widely used and well-established lines, WTC11 (Kreitzer et
161 al., 2013; Liu et al., 2017; Tian et al., 2019), an induced pluripotent stem cell (iPSC) line,
162 and H1 (Thomson et al., 1998), an embryonic stem cell (ESC) line. For the chimpanzee
163 representatives, we chose two robust iPSC lines used in previous studies: C3649 and Pt5-
164 C (Gallego Romero et al., 2015; Ryu et al., 2018) (Table S1).
165
166 To identify genes that modify cellular growth and survival, we infected each cell line with
167 the genome-wide lentiviral hCRISPRi-v2 sgRNA library (Horlbeck et al., 2016, Table S2)
168 (5 sgRNAs/gene), selected for sgRNA-expressing cells with puromycin, cultured cells for
169 10 days, and quantified sgRNA enrichment and depletion by high-throughput sequencing
170 (Table S3). While hCRISPRi-v2 was designed to target the human genome, 77.4% of
171 sgRNAs perfectly matched targets in the chimpanzee reference genome (panTro6);
172 sgRNAs with mismatches were not considered for analyses of species differences (Figure
173 S1A, STAR methods). Across all four screens, we observed robust depletion of sgRNAs
174 targeting common essential genes and enrichment of sgRNAs targeting proliferation-
175 suppressor genes. Analysis of technical and biological replicates revealed strong sgRNA
176 correlations for replicates of the same cell line (Pearson's $r = 0.80$ to 0.97, Figure 1B) and
177 for different cell lines within species ($r = 0.69$ to 0.83). In addition, all four genetic screens
178 sensitively and precisely distinguished Dependency Map (DepMap) common essential and

179   nonessential genes (Blomen et al., 2015; Hart et al., 2014), recalling 82.9% to 92.6% of
180   common essential genes at 95% precision (Figure 1C).
181
182   We next sought to identify genes with species-specific effects on cellular proliferation. To
183   do so, we utilized MAGeCK (Li et al., 2014) and developed a bootstrapping-based method
184   that accounted for both the number of significantly enriched or depleted sgRNAs targeting
185   a gene and the magnitude of sgRNA $\log_2$ fold-change (Figures S1B-D, STAR methods).
186   While the large majority of essential genes were shared between species (Figure 1B), we
187   identified 583 candidate species-specific essential genes and 202 candidate species-
188   specific proliferation-suppressor genes (Figure 1D). Importantly, this approach identified
189   far fewer candidate genes exclusively shared between one individual of each species (n =
190   3 to 12 genes, Figure 1B), highlighting the influence of species on gene essentiality. These
191   results establish a CRISPRi-based approach that overcomes both technical noise in
192   genome-scale screening and variability between PSC lines to reveal candidate species
193   differences.
194
195   **Human and chimpanzee can be distinguished by genetic dependencies**
196
197   We next sought to validate candidate species differences across multiple independently-
198   derived human and chimpanzee PSCs to distinguish species differences from those driven
199   by individual variation (Cahan and Daley, 2013; Kilpinen et al., 2017; Prado-Martinez et
200   al., 2013), adaptation to cell culture (Baker et al., 2007), or somatic cell reprogramming
201   (Merkle et al., 2017). We engineered new CRISPRi stem cell lines from four human
202   (H20961B, H21792A, H23555A, H28126B) and four chimpanzee (C3624K, C8861G,
203   C40280L, C40290F) individuals. To minimize technical variation, we selected cell lines
204   with normal karyotypes that were reprogrammed with identical protocols (Table S1) and
205   maintained in identical media. Furthermore, cell lines from both species were previously
206   shown to differentiate into all three germ layers via teratoma formation and embryoid body
207   assays, functionally validating pluripotency (Gallego Romero et al., 2015). Finally, the
208   human and chimpanzee lines shared comparable pluripotency scores with strongly
209   overlapping patterns of H3K27me3 and H3K27ac at pluripotency genes (Gallego Romero
210   et al., 2015) and similar transcriptional trajectories of differentiation (Blake et al., 2018),
211   suggesting the lines are in a comparable state of pluripotency. We analyzed copy number
212   variation using CaSpER (Serin Harmanci et al., 2020) and genome sequencing coverage to
213   rule out the presence of large duplications or deletions (Figure S2). In addition, we assessed
214   CRISPRi cell lines for p53-responsiveness by measuring sensitivity to nutlin-3a, a small
215   molecule MDM2 inhibitor that induces p53-dependent autophagy and apoptosis
216   (Setoguchi et al., 2016; Vassilev et al., 2004). All 11 new human and chimpanzee lines
217   plus WTC11 and H1 were MDM2/p53-responsive, while C3649 and Pt5-C, the
218   chimpanzee lines used for genome-scale screening, were nonresponsive to MDM2/p53
219   perturbations (Figures S1E and S1F).
220
221   To enable secondary screening, we designed a comparative essential validation (CEV-v1)
222   library consisting of 7,847 sgRNAs targeting the transcriptional start sites of 963 genes
223   from our genome-scale datasets (8 sgRNAs/gene, STAR methods) and 1,845 negative-

224 control sgRNAs (Figure 2A; Figure S3, Table S4). Due to the scalability of pooled
225 screening, we targeted an inclusive set of genes with significant or suggestive differences
226 between species in the primary screens as well as gene families with notable evolutionary
227 histories (Dennis and Eichler, 2016; Pontis et al., 2019). To reduce human-specific bias,
228 we required that every sgRNA in CEV-v1 perfectly match target sites in the human (hg38)
229 and chimpanzee (panTro6) reference genomes (McKenna and Shendure, 2018). In total,
230 we performed 16 CRISPRi screens the CEV-v1 sgRNA library (Figure 2A, Table S5). The
231 validation screens were performed in the four newly constructed CRIPSRi PSC lines of
232 each species. In addition, we retested three of the four PSC lines used for genome-scale
233 screening (Pearson's $r = 0.76$ to 0.89) and performed biological replicate screens in separate
234 laboratories for five cell lines (3 human lines, 2 chimpanzee lines, $r = 0.70$ to 0.92).
235 Notably, hierarchical clustering of cell lines by the similarity of their sgRNA profiles
236 separated all the human (including ESCs and iPSCs) from all the chimpanzee individuals
237 (Figure 2B). Decomposition of each cell line's sgRNA profile by principal component
238 analysis also grouped individuals by species, with the main axes of variation relating to
239 shared changes in sgRNA representation over time (PC1) and species-specific changes
240 (PC2) (Figure 2C). Together, our findings show that stem cells from humans and
241 chimpanzees can be distinguished by their responses to genetic perturbations.
242
243 **Molecular nature of core species-specific genetic dependencies**
244
245 We next sought to identify genes underlying the differences between human and
246 chimpanzee sgRNA profiles. Using generalized linear models borrowed from DE-seq2
247 (Love et al., 2014) we identified 1,133 sgRNAs with evidence for differences between
248 species (1% false discovery rate (FDR), |chimpanzee−human log$_2$ fold-change| ≥ 0.5),
249 while negative-control sgRNAs were tightly distributed around zero (Figure 2D). Using α-
250 RRA (Li et al., 2014) to combine sgRNA P-values, we found 75 genes with robust species-
251 specific effects on cellular proliferation at a 1% FDR (Figure 2E-G; STAR methods). This
252 substantial reduction in the number of significant genes from the CEV-v1 candidate gene
253 pool was the result of a combination of factors: 1) the use of more stringent statistical
254 thresholds, 2) a fraction of genes that replicated in validation screens of the original cell
255 lines but not in the additional cell lines 3) the exclusion of genes whose effects on cellular
256 proliferation depended on *TP53* status. Together, these findings reveal a stringent set of
257 species-specific genetic dependencies that emerged in recent human and chimpanzee
258 evolution.
259
260 We first explored whether species-specific genetic dependencies could relate to changes in
261 the coding sequence or regulation of the target genes themselves that might suggest new
262 species-specific activities of these genes. Several genes in the set exhibited unexpected
263 coding sequence changes. For example, ASPM, which causes microcephaly when mutated,
264 contains protein domains with signatures of positive selection in the human lineage (Evans
265 et al., 2004; Kouprina et al., 2004; Zhang, 2003) and was essential in human but not
266 chimpanzee PSCs. Similarly, KATNA1, which physically interacts with ASPM to promote
267 microtubule disassembly at mitotic spindle poles (Jiang et al., 2017), contains a nearly
268 fixed modern human-specific mutation that is distinct from the Neanderthal and

269   chimpanzee allele (Kuhlwilm and Boeckx, 2019) and acted as a suppressor of proliferation
270   in chimpanzee but not human cells. However, these examples were exceptions, and
271   signatures of adaptive selection, as well as overall non-synonymous substitutions, were
272   depleted among the set of 75 species-specific genetic dependencies compared to the
273   genome wide distribution ($p < 0.01$, $p < 10^{-6}$, respectively, Kolmogorov–Smirnov test,
274   Figure S4A-B). Several genes with divergent genetic dependencies also displayed
275   quantitative gene expression changes. For example, *MTCH2*, a gene involved in
276   mitochondrial metabolism and apoptosis (Gross, 2016) displayed significantly higher
277   expression in human PSCs (fold change = 1.28, FDR $< 10^{-3}$) and was specifically essential
278   in human PSCs. In contrast, *ACAT2*, a gene involved in lipid metabolism, exhibited
279   significantly higher expression in chimpanzee PSCs (fold change = 2.73, FDR $< 10^{-6}$), but
280   was also specifically essential in human cells. Despite these examples, the 75 gene set was
281   also depleted for species differences in gene expression ($P = 0.035$, Figure S4C). Together,
282   these analyses suggest that coding or regulatory changes do not account for the majority of
283   species differences and that a multitude of indirect effects may underlie divergent
284   dependencies (Liu et al., 2019b).

285

286   We next asked whether species-specific genetic dependencies involved groups of genes
287   known to interact, a pattern that could suggest divergent requirements for conserved
288   pathways. As essentiality phenotypes are typically shared among genes within known
289   functional modules (Kim et al., 2022; Wainberg et al., 2021), such coherence could also
290   provide an additional test of internal consistency. Indeed, functionally related genes
291   emerged with consistent patterns of depletion or enrichment within each species. Analysis
292   using the STRING database (Szklarczyk et al., 2021) revealed an enrichment for protein-
293   protein interactions ($p < 10^{-6}$) and components of several well established biological
294   processes (Figure 3A). For example, we observed that all five core components of the
295   UFMylation pathway (*UFM1, UFL1, UFC1, UBA5, DDRGK1*) were essential only in
296   human PSCs (Figure S4D). By contrast, all four subunits of the MOZ histone
297   acetyltransferase complex (*KAT6A, BRPF1, ING5, EAF6*) acted as proliferation
298   suppressors in chimpanzee PSCs (Figure S4D). Accessory proteins to the vacuolar-type
299   ATPase (*ATP6AP1, ATP6AP2*) and the highest ranking DepMap co-dependent gene
300   *WDR7* (Tsherniak et al., 2017), were specifically essential in human PSCs, whereas core
301   subunits were essential in both species (Figure 3B). Strikingly, human PSCs were robust
302   to depletion of cell cycle regulators cyclin-dependent kinase 2 (*CDK2*), its activating
303   partner *Cyclin E1* (*CCNE1*), and cyclin-dependent kinase 4 (*CDK4*). For all three genes,
304   we observed at least six sgRNAs that were essential across six chimpanzee individuals but
305   nonessential across six human individuals (Figure 3C).

306

307   The consistent depletion of many sgRNAs targeting the same gene and multiple genes
308   involved in the same biological process indicates that off-target activity is unlikely to
309   explain proliferation differences between species. In principle, species-specific differences
310   in our CRISPRi screens could also result from differential effectiveness of CRISPRi-
311   mediated transcriptional repression (e.g., due to histone occupancy or transcriptional start
312   site variability). To evaluate this possibility, we measured the efficacy of sgRNA-mediated
313   repression for several candidate genes (*CDK2*, *CCNE1*, and *RBL1*). In all cases,

8

314 measurements of transcript abundance by qRT-PCR revealed >90% knockdown in both
315 species (Figure 4D, Table S6), suggesting that proliferation differences were not driven by
316 incomplete knockdown efficiency in one species. In summary, these results highlight the
317 ability of our screening approach to isolate biologically meaningful networks of genes that
318 mediate species differences in cell behavior when perturbed, in contrast to gene expression
319 profiling, which often reveals a complex mixture of both direct and indirect effects.
320
321 **Genetic perturbations elicit divergent cellular responses**
322
323 While both our primary screen and validation screens measured growth and survival,
324 changes in proliferation can reflect a wide range of cellular phenotypes, from
325 differentiation to growth factor signaling. We first investigated the growth advantage of
326 chimpanzee cells depleted for components of the MOZ histone acetyltransferase complex.
327 MOZ acetylates histone H3 at lysines 9 and 14, and knockout mice are embryonic lethal at
328 E14.5 due to defects in hematopoiesis (Katsumoto et al., 2006; Ullah et al., 2008; Yang,
329 2015). Given the role of the MOZ complex in epigenetic modifications, we hypothesized
330 that there would be species differences in gene expression response. We performed
331 transcriptional profiling of human and chimpanzee cells infected with sgRNAs targeting
332 *BRPF1* or *KAT6A*, normalized to wild-type cells of the same PSC line (Figure 3D, Table
333 S7). Expression changes were strongly correlated between the two perturbations with
334 Pearson's correlation coefficient 0.80 in human cells and 0.83 in chimpanzee cells. Gene
335 ontology enrichment analyses of expression changes combined across both sgRNA
336 perturbations revealed that human cells upregulated genes involved in TGF-beta signaling,
337 cell differentiation, and morphogen activity upon MOZ depletion (Figure S5). In contrast,
338 chimpanzee cells overexpressed genes involved in mTORC1 signaling and Myc targets,
339 consistent with their species-specific growth advantage. In both species, we observed a
340 transcriptional signature consistent with heterogeneous loss of pluripotency. Bulk
341 expression levels of key pluripotency genes *OCT4*, *SOX2*, and *NANOG* were largely
342 unchanged or slightly higher in sgRNA containing cells. However, a broad range of marker
343 genes for multiple germ layers were upregulated. Both species upregulated markers
344 associated with primary ectoderm (*TRIM33*, *TUBB3*), endoderm (*AFP*, *FOXH1*,
345 *CYP26A1*), and mixed lineages (*PDGFRA*, *OTX2*) (Maguire et al., 2013). However, human
346 cells selectively upregulated additional markers of ectoderm (*GBX2*, *MEIS2*), endoderm
347 (*NTS*, *TLE2*, *CER1*), and mixed lineages (*KDR*) compared to chimpanzee cells. Thus, we
348 propose that the MOZ complex plays a conserved role in maintaining an epigenetic barrier
349 to differentiation for both species (Ciceri et al., 2022). However, upon loss of MOZ-
350 mediated histone acetylation, human cells activate expression of a wider range of
351 differentiation markers, suggesting that species differences in epigenetic potential may
352 exist pluripotent cells.
353
354 We next investigated the human-specific sensitivity to loss of *ATP6AP1* and *ATP6AP2*.
355 ATP6AP1 and ATP6AP2 are accessory proteins to the lysosomal V-type ATPase. As the
356 main proton pump responsible for maintaining the pH gradient of the lysosome, non-
357 duplicated core subunits of the V-ATPase were essential in both species, as expected,
358 (Figure 3B). Cryo-electron microscopy of the V-ATPase complex has implicated

359 ATP6AP1 in the assembly of the V_0 complex of the V-ATPase (Wang et al., 2020). In
360 addition, ATP6AP1 is comprised of a transmembrane helix and an extensive luminal
361 domain that bears extensive structural homology to lysosomal-associated membrane
362 proteins (LAMPs) and forms extensive contacts with ATP6AP2. Staining with
363 LysoTracker Red and LysoSensor green in *ATP6AP1* depleted cells revealed no significant
364 defects in maintenance of lysosomal pH (Figure S6). These results are consistent with the
365 core function of V-ATPase being strictly essential. However, loss of *ATP6AP1* has also
366 been implicated in major cellular signaling pathways that are mediated by the lysosome
367 (Jewell et al., 2013; Zhou et al., 2009; Zoncu et al., 2011). Thus, we performed a western
368 blot to measure phosphorylation of ribosomal protein RPS6 (pS6), a well-established
369 downstream effector of mTORC1 activity. Depletion of *ATP6AP1* or *ATP6AP2* resulted in
370 diminished pS6 signal in both species. However, pS6 was selectively abolished in human
371 cells depleted for *ATP6AP1* (Figure 3E). These data thus link the human-specific growth
372 defect of *ATP6AP1* sgRNAs observed in our pooled screens to an increased reliance of
373 human cells on ATP6AP1-mediated mTORC1 signaling.

374

375 **Human PSCs are robust to depletion of CDK2 and Cyclin E**

376

377 Based on the enrichment of genes that regulate cell cycle progression among species-
378 specific genetic dependencies, we next connected the growth phenotypes observed upon
379 depletion of cell cycle factors to more precise cell cycle defects (Figure 4A). To do so, we
380 measured the proportion of cells in G1, S-phase and G2/M via incorporation of the
381 thymidine analogue 5-ethynyl-2′-deoxyuridine (EdU) and Hoechst, a DNA-binding dye.
382 Consistent with the early mammalian embryo, PSCs undergo rapid cell cycle progression
383 with a shortened G1 phase compared to somatic cells (Becker et al., 2006). For wild-type
384 cells, only ~10% of cells were classified in G1 phase (Figure 4B). However, the absolute
385 fraction of G1 cells was influenced by environmental factors such as confluence and
386 nutrient availability. Therefore, we measured the effect of CRISPRi-mediated gene
387 repression in an internally controlled co-culture, with wild-type cells (GFP-) and sgRNA-
388 expressing cells (GFP+) mixed within the same well. Knockdown of *CDK2* or *Cyclin E1*
389 in chimpanzee PSCs led to a roughly two-fold accumulation of cells in G1 (Figure 4C; *P*
390 $< 10^{-3}$ for both), consistent with the well-established role of Cyclin E1-Cdk2 in regulating
391 the G1/S transition. By contrast, knockdown of *CDK2* in human PSCs had no effect on cell
392 cycle progression, and knockdown of *Cyclin E1* produced only a limited accumulation of
393 G1 cells. We confirmed that these differences were not mediated by incomplete sgRNA-
394 mediated knockdown in human PSCs (Figure 4D). Thus, our data suggest that human PSCs
395 are less dependent on Cyclin E1-Cdk2 for G1/S phase transition than chimpanzee PSCs.

396

397 Cyclin E1-Cdk2 is a central regulator of the G1/S cell cycle transition (Hochegger et al.,
398 2008) and is commonly essential (Pacini et al., 2021) and frequently dysregulated across
399 human cancer cell lines (Hwang and Clurman, 2005). In contrast, $CDK2^{-/-}$ knockout mice
400 are fully viable and develop normally, though with reduced body size (Berthet et al., 2003;
401 Ortega et al., 2003). Subsequent studies showed that cell cycle progression could be
402 rescued in the absence of Cyclin E1-Cdk2 by Cyclin A-Cdk1 and Cyclin E-Cdk1 activity
403 (Aleem et al., 2005; Satyanarayana and Kaldis, 2009). Therefore, we reasoned that human

404 cells might compensate for the loss of Cyclin E1-Cdk2 via stronger Cyclin A2-Cdk1
405 activity, as cyclin homologs Cyclin E2 and Cyclin A1 are not expressed in PSCs.
406 Consistent with this model, *CDK1* was more highly expressed in human PSCs (FDR < 10^{-2}
407), while *CDK2* and *Cyclin E1* were more highly expressed in chimpanzee PSCs (FDR <
408 10^{-3}) (Figure 4E; Figure S7). As a functional test, we overexpressed *CDK1* in chimpanzee
409 PSCs in conjunction with sgRNA-mediated repression of *CDK2* or *Cyclin E1* and
410 quantified the progression of cells thru G1 phase. We found that 2.5-fold overexpression
411 of *CDK1* was sufficient for rescuing the sensitivity of chimpanzee PSCs to *CDK2* or *Cyclin*
412 *E1* depletion and accelerated progression through G1/S phase transition (Figure 4F-G).
413
414 Next, we extended our co-culture studies to additional cell cycle regulators with known
415 interactions with Cyclin E-Cdk2. Given the dependence of chimpanzee PSCs on cyclin E-
416 Cdk2, we reasoned that repression of an inhibitor of this cyclin-Cdk complex might have
417 species-specific effects on cell cycle progression. We first investigated the consequences
418 of repressing retinoblastoma-like 1 (*RBL1*/p107), a tumor suppressor homologous to
419 retinoblastoma protein (*RB*). Rbl1, like Rb, classically represses cell cycle via inhibition of
420 E2F transcription factors (Rubin et al., 2020; Shirodkar et al., 1992; Zatulovskiy et al.,
421 2020). However, E2F is de-repressed in rapidly-dividing stem cells compared to other cell
422 types due to the need for rapid cell cycling (Liu et al., 2019a). Rbl1 also possesses an ability
423 unique among Rb family proteins to directly inhibit the kinase activities of cyclin A/E-
424 Cdk2 (Zhu et al., 1995). Accordingly, we observed that repression of *RBL1* but not *RB*
425 resulted in faster growth and a reduction in the fraction of cells in G1 in both species
426 (Figure 4C). However, *RBL1* effects were larger for chimpanzee cells (P < 0.01). Given
427 the accumulation of chimpanzee PSCs in G1 upon repression of *Cyclin E* or *CDK2* (Figure
428 4C), these results further support a model in which cyclin E-Cdk2 exerts greater control
429 over G1/S transition in chimpanzee compared to human PSCs.
430
431 To further link regulation of Cdk1/2 to species divergence in cell cycle progression, we
432 focused on family with sequence similarity 122A (*FAM122A*) (Liu et al., 2021; Zhou et
433 al., 2020), a chimpanzee-specific essential gene. FAM122A acts as an inhibitor
434 phosphatase PP2A-B55α (Fan et al., 2016), which in turn acts in opposition to Cdk1 and
435 Cdk2 by dephosphorylating key substrates such as Wee1 and Cdc25 (Mochida et al., 2009)
436 (Figure 3A). We observed that loss of *FAM122A* phenocopied loss of *CDK2* and led to
437 accumulation of G1 cells in chimpanzee PSCs, but not in human (Figure 4C; *P* < 0.05).
438 Our results suggest that higher endogenous *CDK1* levels could overcome *FAM122A* loss
439 and PP2A phosphatase activation to promote cell cycle re-entry in human PSCs. However,
440 the balance of kinase and phosphatase activity was more sensitive to perturbation in
441 chimpanzee cells, as *CDK2* repression or activation of PP2A led to a delayed G1/S
442 transition.
443
444 Finally, we further examined species differences in PSC cell cycle progression using
445 pharmacological approaches. Based on prior literature (Li et al., 2020), we tested the
446 interaction between *FAM122A* and prexasertib, a Chk1 inhibitor (CHK1i) currently
447 undergoing phase II oncology trials (Byers et al., 2021; Gatti-Mays et al., 2020; Lampert
448 et al., 2020). As with cancer cells, the rapid cell divisions in PSCs render them sensitive to

449 replication stress and DNA damage, conferring vulnerability to prexasertib. As expected,
450 *FAM122A* knockdown PSCs of both species were resistant to prexasertib (Figures 4H; Li
451 et al., 2020). However, with no sgRNA present, wild-type human PSCs were more acutely
452 sensitive to Chk1 inhibition compared to chimpanzee (Figure 4I). These data suggest that
453 chimpanzee PSCs potentially enforce a more robust S phase and G2/M checkpoint
454 compared to human PSCs.
455
456 **Cell cycle perturbations alter neural progenitor cell expansion**
457
458 We wondered whether the molecular differences that we observed between species would
459 also manifest in differentiated cell types. As differences in G1/S regulation have long been
460 hypothesized as an evolutionary mechanism for changing brain size (Dehay and Kennedy,
461 2007; Lukaszewicz et al., 2005; Pilaz et al., 2009; Taverna et al., 2014), we investigated
462 whether human-specific robustness to depletion of cell cycle factors would persist in neural
463 progenitor cells (NPCs). Previous studies have established both the necessity and
464 sufficiency of genes promoting G1/S transition for proliferative NPC divisions in animal
465 model systems (Calegari et al., 2005; Lange et al., 2009, 2009; Lim and Kaldis, 2012;
466 Lukaszewicz et al., 2005; Nonaka-Kinoshita et al., 2013; Pilaz et al., 2009). However, it is
467 not known whether human NPCs possess recently evolved characteristics that imbue them
468 with an enhanced ability to maintain proliferative divisions. We generated CRISPRi human
469 and chimpanzee NPCs and assessed how depletion of *Cyclin E1*, *CDK2*, *RBL1*, and
470 *FAM122A* affected cell cycle progression and self-renewal (Figure 5A-D; Figure S8A-C).
471 In contrast to PSCs, NPCs undergo substantially slower progression through cell cycle,
472 with ~50% of cells in G1 phase compared to ~10% in PSC (Figure 5B). Nonetheless,
473 knockdown of *Cyclin E1* ($P < 0.05$) or *CDK2* ($P < 10^{-3}$) caused an additional accumulation
474 of chimpanzee, but not human, NPCs in G1 (Figure 5C). Meanwhile, *RBL1* knockdown
475 increased NPC proliferation and reduced the fraction of G1 cells in both human and
476 chimpanzee (Figure 5C). Lastly, knockdown of *FAM122A* resulted in G2/M accumulation
477 in chimpanzee but not human NPCs (Figure 5D), implying a greater role for PP2A
478 activation at G2 in chimpanzee NPCs compared to PSCs. Our results suggest that the
479 increased robustness of human NPCs to depletion of regulators of G1/S progression could
480 potentially bias human cells towards prolonged proliferative divisions, as has been
481 proposed by developmental models.
482
483 **Evolutionary origin of molecular species-differences**
484
485 To determine the evolutionary origin of human- and chimpanzee-specific genetic
486 dependencies, we extended our comparative studies to orangutan PSCs (Field et al., 2019).
487 While humans and chimpanzees diverged roughly seven million years ago (Langergraber
488 et al., 2012), orangutans diverged from other great apes 13-18 million years ago (Glazko
489 and Nei, 2003). Thus, we could infer by maximum parsimony that any genetic
490 dependencies shared between orangutans and chimpanzees but not humans were likely to
491 have been present in the common ancestor and subsequently diverged in the human lineage.
492 We performed three-way species comparisons across genes representing several biological
493 processes with coherent species differences in our dataset using sgRNAs with perfectly-

12

494   matched targets in all three species. For two sgRNAs targeting *CDK2*, we observed a
495   significant depletion of sgRNA-expressing cells over the course of ten days in both
496   chimpanzee and orangutan PSCs (Figure 6A). In contrast, no such depletion was observed
497   in human PSCs. We further confirmed that the differences we observed were not due to
498   differences in sgRNA activity, as knockdown efficiency exceeded 90% in all three species.
499   In addition, we further observed human-specific robustness to repression of *CDK4* (Figure
500   6B) and *Cyclin E1* (Figures S9A and S9B). Based on these data, we inferred that robustness
501   to perturbations of the G1/S transition evolved along the human lineage, otherwise
502   dependence on *CDK2*, *CDK4*, and *Cyclin E1* would have had to evolve on two separate
503   occasions in the chimpanzee and orangutan lineages with the same direction of effect for
504   each gene. Next, we evaluated the human-specific sensitivity to repression of *ATP6AP1*.
505   We observed that the *ATP6AP1* sensitivity was not shared by chimpanzee or orangutan
506   PSCs, suggesting that altered responses to cellular metabolism, including the increased
507   reliance on ATP6AP1 for mTORC1 signaling that we observed also evolved along the
508   human lineage (Figure 6C).
509
510   By contrast, repression of *KAT6A* promoted proliferation in chimpanzee PSCs but not in
511   human or orangutan PSCs, arguing that this molecular feature was derived in chimpanzees
512   (Figure 6D). Similarly, sensitivity to *UFL1* repression was common to human and
513   orangutan PSCs but diverged in chimpanzee PSCs (Figure 6E). The bidirectional
514   polarization of orangutan PSCs towards both human and chimpanzee PSCs, depending on
515   biological pathway, provides an additional line of evidence that the species-specific genetic
516   dependencies that we observed did not arise from two distinct pluripotency states in human
517   and chimpanzee PSCs. If this were the case, the orangutan PSCs should consistently
518   polarize more closely towards one species and not the other. In sum, our data indicate that
519   distinct genetic dependencies arose recently in both the human and chimpanzee lineages,
520   highlighting the importance of experimentally defining which cellular and molecular
521   differences are human derived to inform our understanding of human evolution.
522
523   **Discussion**
524
525   Loss-of-function screens have provided deep insights into the genes that regulate the
526   development of model organisms. Here, we extended the scope of genetic screens to human
527   and chimpanzee PSCs and examined whether the requirements for essential genes could
528   differ in closely related species. By performing paired genome-wide CRISPRi screens, we
529   uncovered a divergent landscape of genetic dependencies. Despite human and chimpanzee
530   PSCs being similar in their cellular morphology, response to *in vitro* differentiation
531   protocols, and core essential-ome, we identified 75 genes with divergent roles in
532   controlling cellular proliferation. We observed that many of these genes were organized in
533   coherent protein complexes and biochemical pathways, a metric of internal consistency
534   that demonstrated the technical quality of our screens. Our data thus comprise a rich
535   resource that interfaces with existing studies of gene regulation and chromatin states and
536   provides a functional genomics guide for future candidate gene approaches.
537

538   Our work further demonstrates the capacity for comparative screening approaches to reveal
539   latent molecular differences between closely-related species. The keys to the success of
540   our approach include: 1) the scalability of CRISPRi sgRNA libraries, which target each
541   gene with multiple unique sgRNAs, enabling the comprehensive and unbiased exploration
542   of species-specific differences in genetic dependencies 2) the ability to design sgRNAs that
543   target conserved genomic sequences in human and chimpanzee cells, and 3) the use of cells
544   lines from multiple individuals of each species to distinguish consistent species differences
545   from individual and technical sources of variation. We found that human and chimpanzee
546   PSCs exhibit differential sensitivity to depletion of key components of cell cycle,
547   lysosomal function, UFMylation, and histone modification. We further applied our
548   comparative screening approach to orangutans, an outgroup to both humans and
549   chimpanzees. By performing a three species comparison, we inferred the evolutionary
550   history of several divergent species-specific molecular phenotypes. We found that
551   robustness to depletion of *CDK2, CDK4,* and *Cyclin E1* and sensitivity to depletion of
552   *ATP6AP1* were unique to humans, and thus likely arose after the last common ancestor of
553   humans and chimpanzees. In contrast, depletion of *KAT6A* and *UFL1* led to changes in
554   growth that were specific to chimpanzees. Thus, our ability to distinguish which species-
555   differences arose within the human lineage is an indicator of their potential relevance to
556   human phenotypic evolution.
557
558   How might the genetic dependencies we observed in PSCs relate to organismal differences
559   that manifest during development? Intriguingly, we found that human-specific robustness
560   to depletion of cell cycle factors persisted in neural progenitor cells. The G1-phase length
561   hypothesis proposes that factors which lengthen G1 duration in NPCs increase the
562   probability of differentiation towards non-proliferative neuronal fates, while factors
563   reducing G1 length promote proliferative self-renewal of NPCs (Calegari et al., 2005;
564   Dehay and Kennedy, 2007; Taverna et al., 2014). Indeed, loss of CDK2 or CDK4 in mouse
565   NPCs prolongs G1 length and causes premature neuronal differentiation at the expense of
566   self-renewal (Lim and Kaldis, 2012). Conversely, exogenous overexpression of *CDK4* and
567   *Cyclin D1* in mouse and ferret reduces G1 length, promotes self-renewing divisions in basal
568   progenitor cells, and results in increased brain size and cortical area, while preserving a
569   structurally normal, six-layered cortex (Nonaka-Kinoshita et al., 2013). These studies
570   underscore the influence of inputs to the G1/S transition on brain expansion during
571   development. However, whether this developmental mechanism changed specifically in
572   recent human evolution remained unexplored. Our demonstration that human NPCs are
573   more likely than chimpanzee NPCs to continue cycling upon equivalent repression of
574   *CDK2* and *Cyclin E1* connects proposed developmental mechanisms to molecular changes
575   that occurred in human evolution. Our results, in concordance with previous studies,
576   support a general framework where a combination of intrinsic developmental tempo and
577   external environmental inputs govern the length of G1-phase in neural progenitor cells
578   (Figure 7A). Factors promoting rapid G1/S transition, such as mitogen signaling and
579   cyclin-CDK activity, will promote neural progenitor self-renewal and lead to an expansion
580   of the progenitor field. Similarly, environmental stressors that lengthen G1-phase such as
581   nutrient limitation and DNA damage can trigger neural progenitor differentiation.
582   Molecular changes that make human NPCs less sensitive to these differentiation-promoting

14

583 signals, as we observed via genetic perturbations, could bias human NPCs to increased
584 proliferation in more complex *in vivo* environments. Future studies can thus assess the
585 response of human and chimpanzee NPCs to a wider range of genetic and physiological
586 perturbations to provide further insights into the evolutionary mechanisms by which the
587 proliferative capacity of NPCs has increased along the human lineage.
588
589 The endeavor to study the molecular basis of human evolution has been compared to
590 searching for needles in a haystack, as human-specific genetic variants and gene expression
591 changes are numerous and predominantly neutral (Varki and Altheide, 2005). By contrast,
592 our finding that human and chimpanzee PSCs exhibit distinct genetic dependencies, even
593 for genes that lack clear expression or protein-coding sequence divergence, provides a
594 complementary approach for isolating recently-evolved functional changes in human gene
595 networks. This conceptual advance mirrors the progression of cancer genetics research
596 from sequencing and transcriptomics efforts such as TCGA (Weinstein et al., 2013) to
597 functional genetics-based efforts such as DepMap (Pacini et al., 2021; Tsherniak et al.,
598 2017). Moreover, while driver mutations can be identified in tumors based on their
599 independent recurrence, human evolution has occurred only once, highlighting the added
600 value of a functional genomics platform. Our approach can be readily applied in
601 differentiated cell types and interfaced with higher dimensional measurements of cell
602 phenotypes (Adamson et al., 2016; Dixit et al., 2016; Feldman et al., 2019), opening the
603 door to future efforts for understanding molecular control of species differences across
604 stages of development.

15

605

606
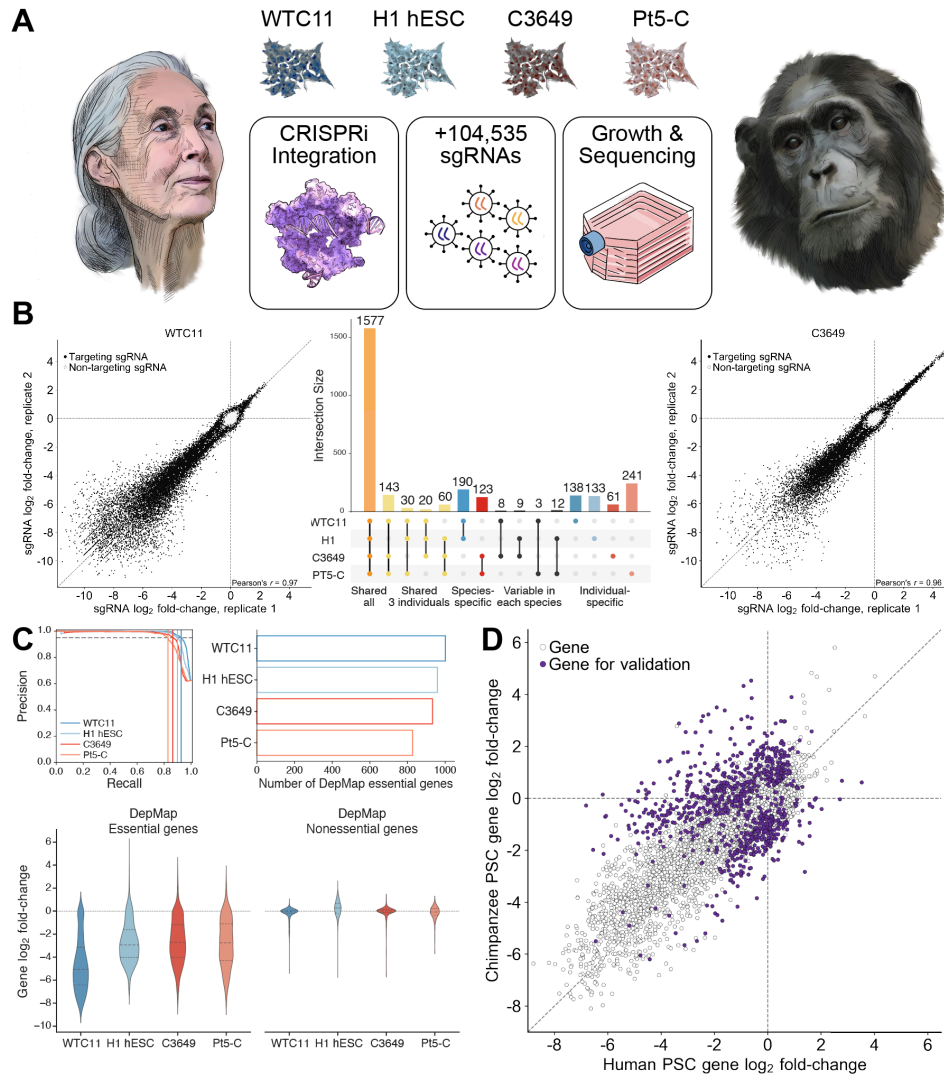
Figure 1. Genome-wide CRISPRi screens in human and chimpanzee stem cells identify candidate species-specific genetic dependencies

(A) Schematic of CRISPRi screening approach. Two human (WTC11 and H1) and two chimpanzee (C3649 and Pt5-C) PSC lines were engineered to express dCas9-KRAB, infected with the lentiviral hCRISPRi-2 sgRNA library, and grown competitively for 10 days. Depleted and enriched sgRNAs were detected by high-throughput sequencing. (B) Scatterplots of sgRNA fold-change for WTC11 and C3649 technical replicates and UpSet plot showing the intersection of essential genes across screens. (C) Precision-recall analysis (top left) for each screen. Precision and recall were determined using DepMap essential and nonessential genes. The number of DepMap essential genes (top right) identified by MAGeCK (5% FDR, $\log_2$ fold-change < -1.5). Distribution of fold-change for DepMap essential (bottom left) and nonessential (bottom right) genes. (D) Species-level gene fold-change across genome-wide CRISPRi screens. Gene-level phenotypes were computed as the mean of the three sgRNAs with the largest absolute fold-change. sgRNAs lacking perfect-match targets in the chimpanzee genome were excluded from analysis.

16
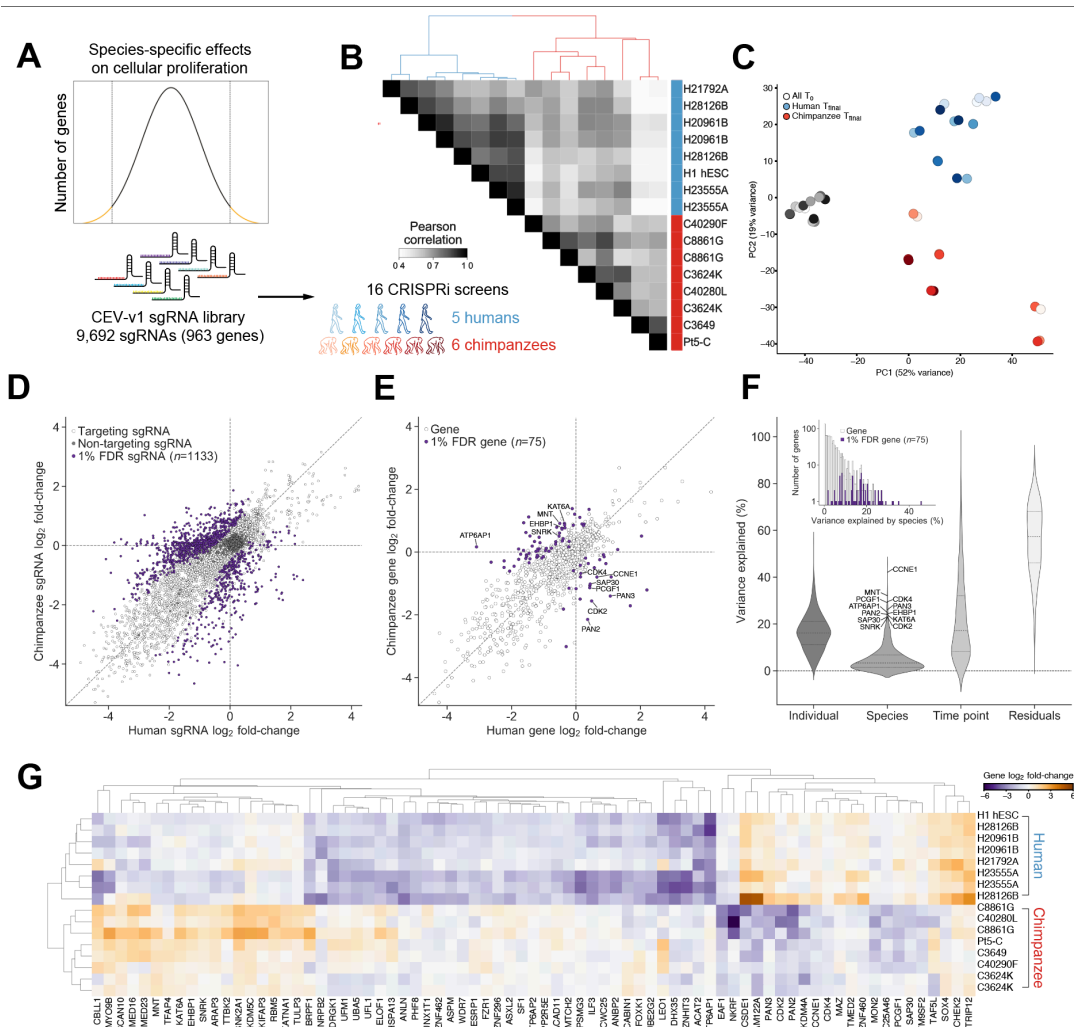
Figure 2. Species-specific genetic dependencies validate across five human and six chimpanzee individuals

(A) Schematic of validation sgRNA library design and CRISPRi screening approach. (B) Heatmap of Pearson correlations and hierarchical clustering for sgRNA profiles across 16 validation CRISPRi screens. Individuals listed twice are replicate screens performed in separate laboratories. (C) Principal component analysis of sgRNA counts at t_0 (black circle) and t_{final} (red and blue circles). (D) Scatterplot of $\log_2$ fold-change of sgRNA counts, weighted and normalized by DESeq2. 1,133 sgRNAs with significant species differences (FDR < 0.01) colored in purple and negative-control sgRNAs colored in dark gray. (E) Species-level gene fold-change across validation CRISPRi screens. Gene-level phenotypes were computed as the mean of the four sgRNAs with the largest absolute fold-change. The 12 genes with the greatest variance in sgRNA fold-change attributable to species are labeled. (F) Dream-variancePartition analysis for quantifying sources of variation in sgRNA counts attributable to individual, species, and timepoint (t_0 vs. t_{final}). (G) Heatmap of gene fold-change and hierarchical clustering for 75 genes with species-specific effects on cellular proliferation across validation CRISPRi screens (1% FDR).

17
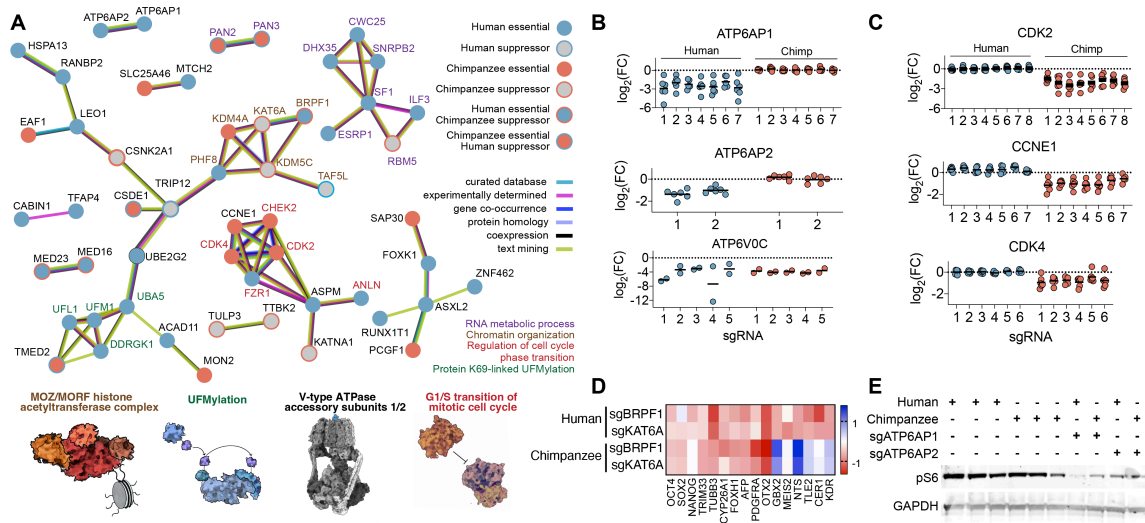
Figure 3. Core species-specific genetic dependencies
(A) Species-specific genetic dependencies with STRING protein-protein associations. Illustrations of pathways and protein complexes with coherent species-specific effects. (B) Strip plots of fold-change for sgRNAs targeting *ATP6AP1*, *ATP6AP2* and *ATP6V0C* (C) *CDK2*, *CCNE1*, and *CDK4*. Each circle represents the sgRNA fold-change for one sgRNA in one human (blue) or chimpanzee (red) individual. Each stripplot contains a variable number of columns, corresponding to the number of significant sgRNAs targeting each gene. (D) Heatmap of RNA-seq expression data for human (WTC11) and chimpanzee (C3649) cells depleted for KAT6A or BRPF1. (E) Western blot for phospho-S6 expression and GAPDH loading control for three wild-type human (H1, 21792A, and 28128B) and three wild-type chimpanzee (3624K, 40280L, and 8861G) cell lines, and cell lines depleted for ATP6AP1 or ATP6AP2 (28128B and 40280L).

18

652

653
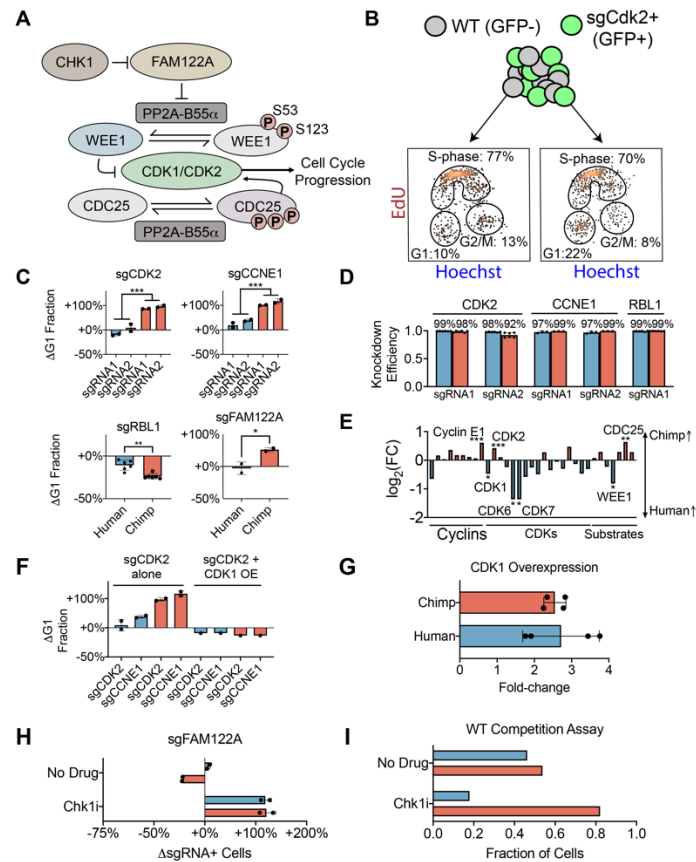
Figure 4. Divergent regulation of cell cycle progression in human and chimpanzee cells

(A) Schematic for Cdk1/Cdk2 regulatory network. Cdk1 and Cdk2 phosphorylate key substrates Wee1 and Cdc25, leading to degradation of Wee1 and activation of Cdc25. Phosphatase PP2A dephosphorylates Wee1 and Cdc25 at the same sites. Chk1 inhibits FAM122A, and FAM122A inhibits PP2A. (B) Cell cycle proportions in chimpanzee wild-type cells (GFP-) and sgRNA containing cells (GFP+) grown in co-culture. (C) Change in the fraction of cells in G1 phase upon knockdown of *CDK2* ($P < 10^{-3}$), *Cyclin E1* ($P < 10^{-3}$), *RBL1* ($P < 10^{-2}$), and *FAM122A* ($P < 0.05$). (D) qRT-PCR measurements of knockdown efficiency in human (blue) and chimpanzee (red) PSCs. (E) Comparative gene expression data from human and chimpanzee PSCs for core cell cycle regulators (* $P < 0.05$, ** $P < 10^{-2}$, *** $P < 10^{-3}$). (F) Change in the fraction of cells in G1 phase upon overexpression of *CDK1* in conjunction with *CDK2* or *Cyclin E1* knockdown. (G) qRT-PCR measurements of the degree of *CDK1* overexpression. (H) Change in the fraction of FAM122A sgRNA containing cells in the presence of no drug or Chk1 inhibitor prexasertib (Chk1i). (I) Fraction of wild-type human (blue) vs. wild-type chimpanzee (red) cells grown in co-culture in the presence of no drug or Chk1i.
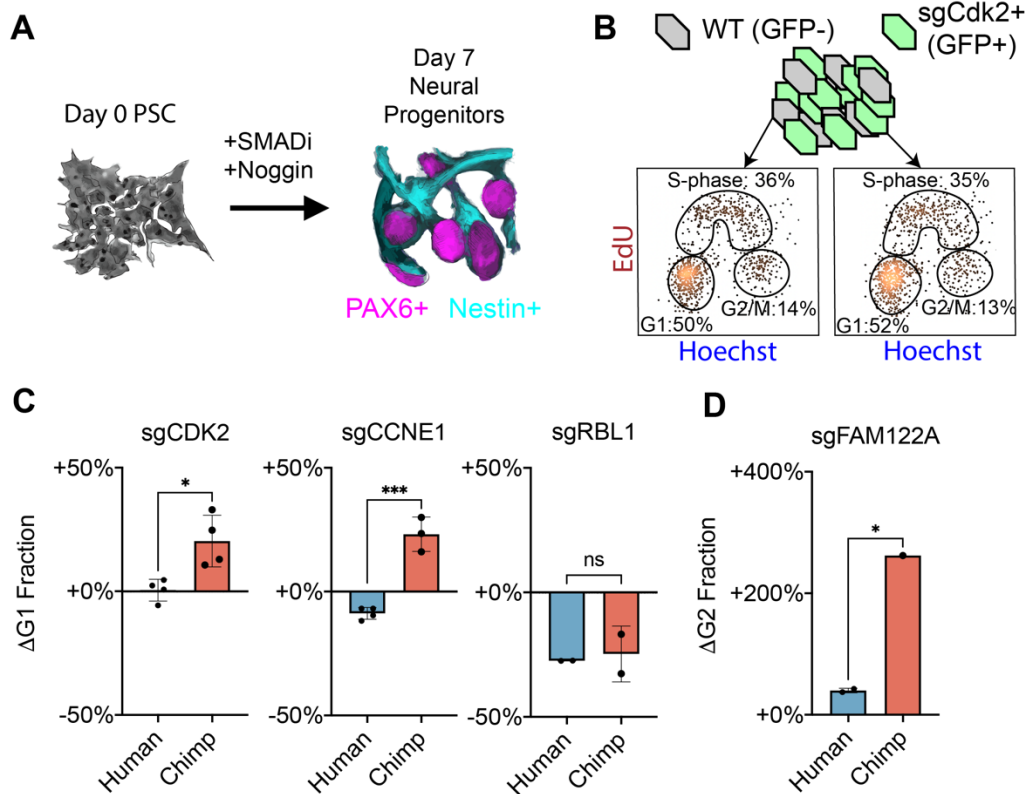
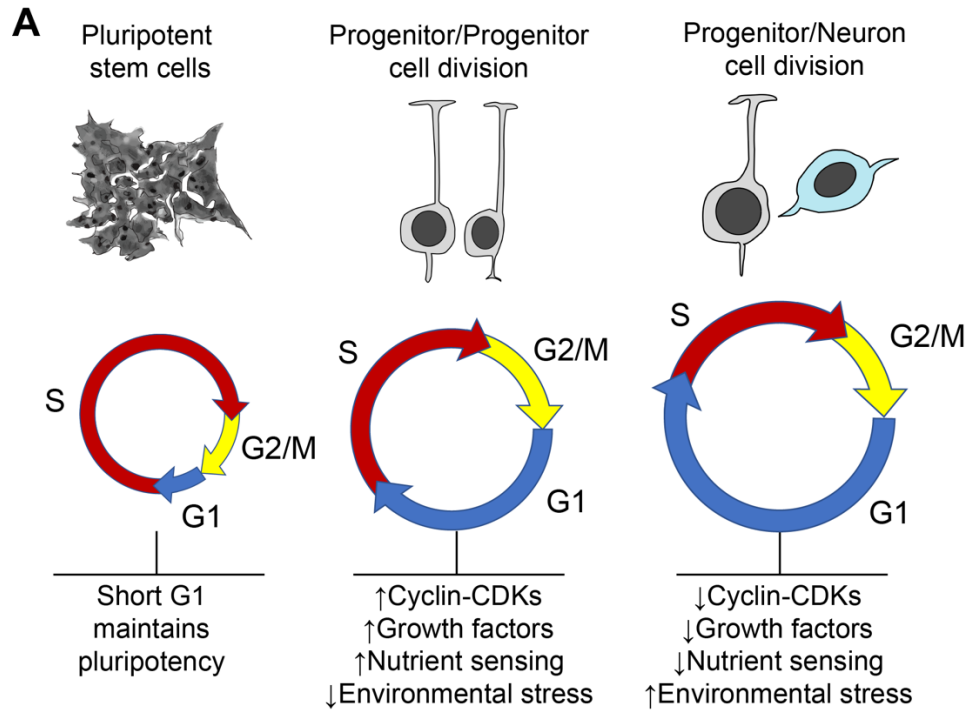**Figure 5. Differentiation into neural progenitor cells**
(A) Schematic for differentiation of PSCs into neural progenitor cells (NPCs). (B) Cell cycle proportions in human wild-type neural progenitor cells (GFP-) and sgRNA containing cells (GFP+) grown in co-culture. (C) Change in the fraction of NPCs in G1 phase upon depletion of *CDK2* ($P < 0.05$), *Cyclin E1* ($P < 10^{-3}$), or *RBL1* (n.s.). (D) Change in the fraction of NPCs in G2 phase upon depletion of *FAM122A* ($P < 0.05$).
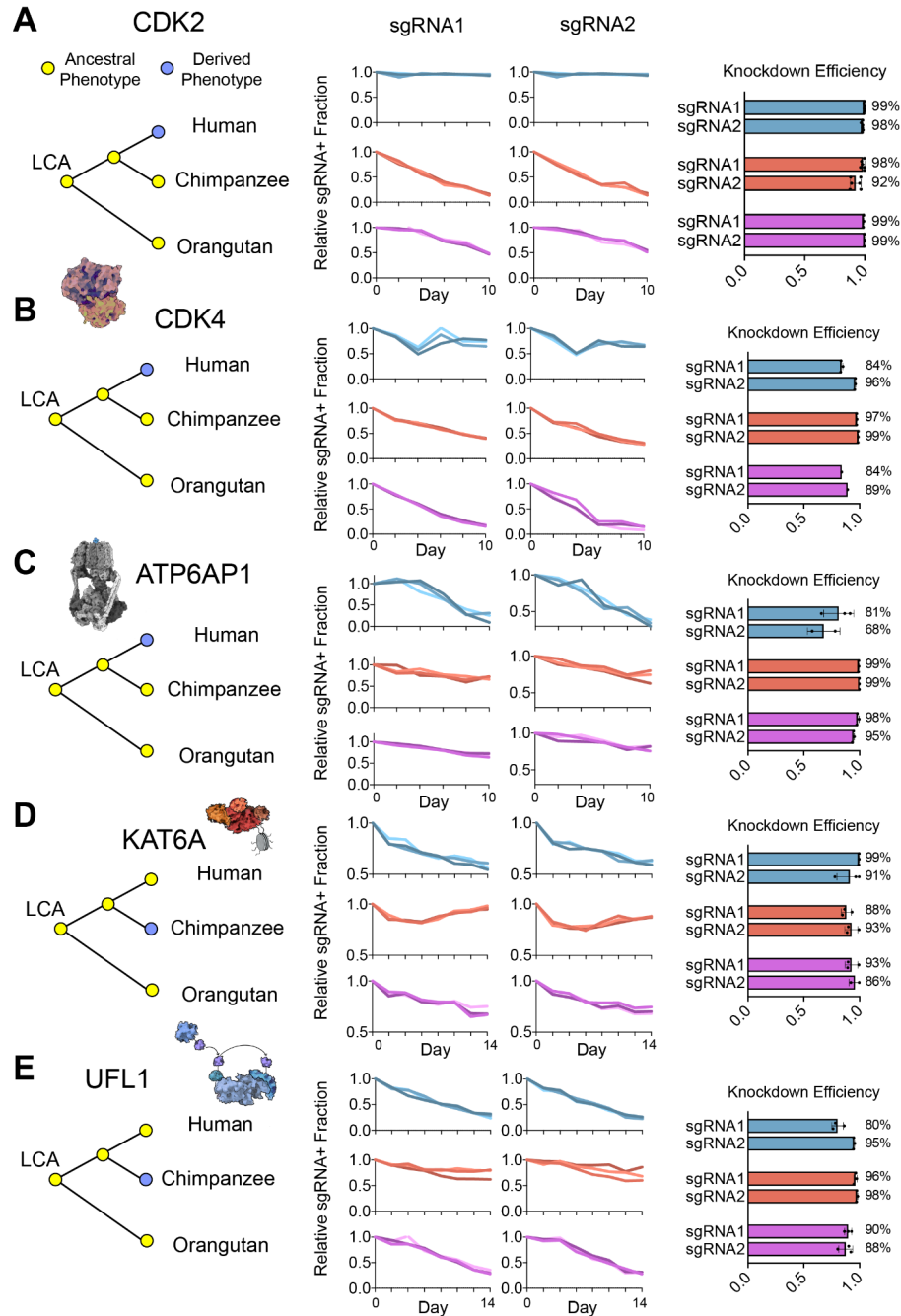
Figure 6. Orangutan PSCs reveal evolutionary origin of species-specific genetic dependencies

(A) Change in the relative fraction of CDK2 sgRNA containing cells over time in human, chimpanzee, and orangutan PSCs. qRT-PCR measurements of sgRNA knockdown efficiency for each sgRNA in all three species. (B-E) Relative sgRNA fraction over time and qRT-PCR measurements for sgRNAs targeting (B) *CDK4*, (C) *ATP6AP1*, (D) *KAT6A*, and (E) *UFL1*.

A

688
689
Figure 7. Model for inputs to neural progenitor differentiation
(A) Schematic for changes in cell cycle length and proportion in pluripotent stem cells and neural progenitor cells with intrinsic and extrinsic inputs that can potentially influence the duration of G1 phase.

694   **References:**

696   Adamson, B., Norman, T.M., Jost, M., Cho, M.Y., Nuñez, J.K., Chen, Y., Villalta, J.E.,
697   Gilbert, L.A., Horlbeck, M.A., Hein, M.Y., et al. (2016). A Multiplexed Single-Cell
698   CRISPR Screening Platform Enables Systematic Dissection of the Unfolded Protein
699   Response. Cell *167*, 1867-1882.e21. https://doi.org/10.1016/j.cell.2016.11.048.

700   Aldea, D., Atsuta, Y., Kokalari, B., Schaffner, S.F., Prasasya, R.D., Aharoni, A.,
701   Dingwall, H.L., Warder, B., and Kamberov, Y.G. (2021). Repeated mutation of a
702   developmental enhancer contributed to human thermoregulatory evolution. Proc. Natl.
703   Acad. Sci. *118*, e2021722118. https://doi.org/10.1073/pnas.2021722118.

704   Aleem, E., Kiyokawa, H., and Kaldis, P. (2005). Cdc2-cyclin E complexes regulate the
705   G1/S phase transition. Nat. Cell Biol. *7*, 831–836. https://doi.org/10.1038/ncb1284.

706   Baker, D.E.C., Harrison, N.J., Maltby, E., Smith, K., Moore, H.D., Shaw, P.J., Heath,
707   P.R., Holden, H., and Andrews, P.W. (2007). Adaptation to culture of human embryonic
708   stem cells and oncogenesis in vivo. Nat. Biotechnol. *25*, 207–215.
709   https://doi.org/10.1038/nbt1285.

710   Becker, K.A., Ghule, P.N., Therrien, J.A., Lian, J.B., Stein, J.L., van Wijnen, A.J., and
711   Stein, G.S. (2006). Self-renewal of human embryonic stem cells is supported by a
712   shortened G1 cell cycle phase. J. Cell. Physiol. *209*, 883–893.
713   https://doi.org/10.1002/jcp.20776.

714   Berthet, C., Aleem, E., Coppola, V., Tessarollo, L., and Kaldis, P. (2003). Cdk2
715   Knockout Mice Are Viable. Curr. Biol. *13*, 1775–1785.
716   https://doi.org/10.1016/j.cub.2003.09.024.

717   Blake, L.E., Thomas, S.M., Blischak, J.D., Hsiao, C.J., Chavarria, C., Myrthil, M., Gilad,
718   Y., and Pavlovic, B.J. (2018). A comparative study of endoderm differentiation in
719   humans and chimpanzees. Genome Biol. *19*, 162. https://doi.org/10.1186/s13059-018-
720   1490-5.

721   Blomen, V.A., Májek, P., Jae, L.T., Bigenzahn, J.W., Nieuwenhuis, J., Staring, J., Sacco,
722   R., van Diemen, F.R., Olk, N., Stukalov, A., et al. (2015). Gene essentiality and synthetic
723   lethality in haploid human cells. Science *350*, 1092–1096.
724   https://doi.org/10.1126/science.aac7557.

725   Boyd, J.L., Skove, S.L., Rouanet, J.P., Pilaz, L.-J., Bepler, T., Gordân, R., Wray, G.A.,
726   and Silver, D.L. (2015). Human-chimpanzee differences in a FZD8 enhancer alter cell-
727   cycle dynamics in the developing neocortex. Curr. Biol. CB *25*, 772–779.
728   https://doi.org/10.1016/j.cub.2015.01.041.

729   Byers, L.A., Navarro, A., Schaefer, E., Johnson, M., Özgüroğlu, M., Han, J.-Y.,
730   Bondarenko, I., Cicin, I., Dragnev, K.H., Abel, A., et al. (2021). A Phase II Trial of

731   Prexasertib (LY2606368) in Patients With Extensive-Stage Small-Cell Lung Cancer.
732   Clin. Lung Cancer S1525-7304(21)00089-9. https://doi.org/10.1016/j.cllc.2021.04.005.

733   Cahan, P., and Daley, G.Q. (2013). Origins and implications of pluripotent stem cell
734   variability and heterogeneity. Nat. Rev. Mol. Cell Biol. *14*, 357–368.
735   https://doi.org/10.1038/nrm3584.

736   Calegari, F., Haubensak, W., Haffner, C., and Huttner, W.B. (2005). Selective
737   lengthening of the cell cycle in the neurogenic subpopulation of neural progenitor cells
738   during mouse brain development. J. Neurosci. Off. J. Soc. Neurosci. *25*, 6533–6538.
739   https://doi.org/10.1523/JNEUROSCI.0778-05.2005.

740   Cerbini, T., Funahashi, R., Luo, Y., Liu, C., Park, K., Rao, M., Malik, N., and Zou, J.
741   (2015). Transcription activator-like effector nuclease (TALEN)-mediated CLYBL
742   targeting enables enhanced transgene expression and one-step generation of dual reporter
743   human induced pluripotent stem cell (iPSC) and neural stem cell (NSC) lines. PloS One
744   *10*, e0116032. https://doi.org/10.1371/journal.pone.0116032.

745   Ciceri, G., Cho, H., Kshirsagar, M., Baggiolini, A., Aromolaran, K.A., Walsh, R.M.,
746   Goldstein, P.A., Koche, R.P., Leslie, C.S., and Studer, L. (2022). An epigenetic barrier
747   sets the timing of human neuronal maturation. 2022.06.02.490114.
748   https://doi.org/10.1101/2022.06.02.490114.

749   Costa, M., Wilson, E.T., and Wieschaus, E. (1994). A putative cell signal encoded by the
750   folded gastrulation gene coordinates cell shape changes during Drosophila gastrulation.
751   Cell *76*, 1075–1089. https://doi.org/10.1016/0092-8674(94)90384-0.

752   Dehay, C., and Kennedy, H. (2007). Cell-cycle control and cortical development. Nat.
753   Rev. Neurosci. *8*, 438–450. https://doi.org/10.1038/nrn2097.

754   Dennis, M.Y., and Eichler, E.E. (2016). Human adaptation and evolution by segmental
755   duplication. Curr. Opin. Genet. Dev. *41*, 44–52.
756   https://doi.org/10.1016/j.gde.2016.08.001.

757   Dickinson, M.E., Flenniken, A.M., Ji, X., Teboul, L., Wong, M.D., White, J.K., Meehan,
758   T.F., Weninger, W.J., Westerberg, H., Adissu, H., et al. (2016). High-throughput
759   discovery of novel developmental phenotypes. Nature *537*, 508–514.
760   https://doi.org/10.1038/nature19356.

761   Dixit, A., Parnas, O., Li, B., Chen, J., Fulco, C.P., Jerby-Arnon, L., Marjanovic, N.D.,
762   Dionne, D., Burks, T., Raychowdhury, R., et al. (2016). Perturb-Seq: Dissecting
763   Molecular Circuits with Scalable Single-Cell RNA Profiling of Pooled Genetic Screens.
764   Cell *167*, 1853-1866.e17. https://doi.org/10.1016/j.cell.2016.11.038.

765   Dutrow, E.V., Emera, D., Yim, K., Uebbing, S., Kocher, A.A., Krenzer, M., Nottoli, T.,
766   Burkhardt, D.B., Krishnaswamy, S., Louvi, A., et al. (2022). Modeling uniquely human

24

767   gene regulatory function via targeted humanization of the mouse genome. Nat. Commun.
768   *13*, 304. https://doi.org/10.1038/s41467-021-27899-w.

769   Enard, W., Przeworski, M., Fisher, S.E., Lai, C.S.L., Wiebe, V., Kitano, T., Monaco,
770   A.P., and Pääbo, S. (2002). Molecular evolution of FOXP2, a gene involved in speech
771   and language. Nature *418*, 869–872. https://doi.org/10.1038/nature01025.

772   Evans, P.D., Anderson, J.R., Vallender, E.J., Gilbert, S.L., Malcom, C.M., Dorus, S., and
773   Lahn, B.T. (2004). Adaptive evolution of ASPM, a major determinant of cerebral cortical
774   size in humans. Hum. Mol. Genet. *13*, 489–494. https://doi.org/10.1093/hmg/ddh055.

775   Fan, L., Liu, M.-H., Guo, M., Hu, C.-X., Yan, Z.-W., Chen, J., Chen, G.-Q., and Huang,
776   Y. (2016). FAM122A, a new endogenous inhibitor of protein phosphatase 2A.
777   Oncotarget *7*, 63887–63900. https://doi.org/10.18632/oncotarget.11698.

778   Feldman, D., Singh, A., Schmid-Burgk, J.L., Carlson, R.J., Mezger, A., Garrity, A.J.,
779   Zhang, F., and Blainey, P.C. (2019). Optical Pooled Screens in Human Cells. Cell *179*,
780   787-799.e17. https://doi.org/10.1016/j.cell.2019.09.016.

781   Fiddes, I.T., Lodewijk, G.A., Mooring, M., Bosworth, C.M., Ewing, A.D., Mantalas,
782   G.L., Novak, A.M., van den Bout, A., Bishara, A., Rosenkrantz, J.L., et al. (2018).
783   Human-Specific NOTCH2NL Genes Affect Notch Signaling and Cortical Neurogenesis.
784   Cell *173*, 1356-1369.e22. https://doi.org/10.1016/j.cell.2018.03.051.

785   Field, A.R., Jacobs, F.M.J., Fiddes, I.T., Phillips, A.P.R., Reyes-Ortiz, A.M.,
786   LaMontagne, E., Whitehead, L., Meng, V., Rosenkrantz, J.L., Olsen, M., et al. (2019).
787   Structurally Conserved Primate LncRNAs Are Transiently Expressed during Human
788   Cortical Differentiation and Influence Cell-Type-Specific Genes. Stem Cell Rep. *12*,
789   245–257. https://doi.org/10.1016/j.stemcr.2018.12.006.

790   Florio, M., Namba, T., Pääbo, S., Hiller, M., and Huttner, W.B. (2016). A single splice
791   site mutation in human-specific ARHGAP11B causes basal progenitor amplification. Sci.
792   Adv. *2*, e1601941. https://doi.org/10.1126/sciadv.1601941.

793   Gallego Romero, I., Pavlovic, B.J., Hernando-Herraez, I., Zhou, X., Ward, M.C.,
794   Banovich, N.E., Kagan, C.L., Burnett, J.E., Huang, C.H., Mitrano, A., et al. (2015). A
795   panel of induced pluripotent stem cells from chimpanzees: a resource for comparative
796   functional genomics. ELife *4*, e07103. https://doi.org/10.7554/eLife.07103.

797   Gaspar-Maia, A., Alajem, A., Meshorer, E., and Ramalho-Santos, M. (2011). Open
798   chromatin in pluripotency and reprogramming. Nat. Rev. Mol. Cell Biol. *12*, 36–47.
799   https://doi.org/10.1038/nrm3036.

800   Gatti-Mays, M.E., Karzai, F.H., Soltani, S.N., Zimmer, A., Green, J.E., Lee, M.-J.,
801   Trepel, J.B., Yuno, A., Lipkowitz, S., Nair, J., et al. (2020). A Phase II Single Arm Pilot
802   Study of the CHK1 Inhibitor Prexasertib (LY2606368) in BRCA Wild-Type, Advanced

803   Triple-Negative Breast Cancer. The Oncologist *25*, 1013-e1824.
804   https://doi.org/10.1634/theoncologist.2020-0491.

805   Gilbert, L.A., Horlbeck, M.A., Adamson, B., Villalta, J.E., Chen, Y., Whitehead, E.H.,
806   Guimaraes, C., Panning, B., Ploegh, H.L., Bassik, M.C., et al. (2014). Genome-Scale
807   CRISPR-Mediated Control of Gene Repression and Activation. Cell *159*, 647–661.
808   https://doi.org/10.1016/j.cell.2014.09.029.

809   Glazko, G.V., and Nei, M. (2003). Estimation of divergence times for major lineages of
810   primate species. Mol. Biol. Evol. *20*, 424–434. https://doi.org/10.1093/molbev/msg050.

811   Gross, A. (2016). BCL-2 family proteins as regulators of mitochondria metabolism.
812   Biochim. Biophys. Acta *1857*, 1243–1246. https://doi.org/10.1016/j.bbabio.2016.01.017.

813   Hart, T., Brown, K.R., Sircoulomb, F., Rottapel, R., and Moffat, J. (2014). Measuring
814   error rates in genomic perturbation screens: gold standards for human functional
815   genomics. Mol. Syst. Biol. *10*, 733. https://doi.org/10.15252/msb.20145216.

816   Heide, M., Haffner, C., Murayama, A., Kurotaki, Y., Shinohara, H., Okano, H., Sasaki,
817   E., and Huttner, W.B. (2020). Human-specific ARHGAP11B increases size and folding
818   of primate neocortex in the fetal marmoset. Science *369*, 546–550.
819   https://doi.org/10.1126/science.abb2401.

820   Hochegger, H., Takeda, S., and Hunt, T. (2008). Cyclin-dependent kinases and cell-cycle
821   transitions: does one fit all? Nat. Rev. Mol. Cell Biol. *9*, 910–916.
822   https://doi.org/10.1038/nrm2510.

823   Hooper, J.E., and Scott, M.P. (1989). The Drosophila patched gene encodes a putative
824   membrane protein required for segmental patterning. Cell *59*, 751–765.
825   https://doi.org/10.1016/0092-8674(89)90021-4.

826   Horlbeck, M.A., Gilbert, L.A., Villalta, J.E., Adamson, B., Pak, R.A., Chen, Y., Fields,
827   A.P., Park, C.Y., Corn, J.E., Kampmann, M., et al. (2016). Compact and highly active
828   next-generation libraries for CRISPR-mediated gene repression and activation. ELife *5*,
829   e19760. https://doi.org/10.7554/eLife.19760.

830   Hrabě de Angelis, M., Nicholson, G., Selloum, M., White, J.K., Morgan, H., Ramirez-
831   Solis, R., Sorg, T., Wells, S., Fuchs, H., Fray, M., et al. (2015). Analysis of mammalian
832   gene function through broad-based phenotypic screens across a consortium of mouse
833   clinics. Nat. Genet. *47*, 969–978. https://doi.org/10.1038/ng.3360.

834   Hwang, H.C., and Clurman, B.E. (2005). Cyclin E in normal and neoplastic cell cycles.
835   Oncogene *24*, 2776–2786. https://doi.org/10.1038/sj.onc.1208613.

836   Jewell, J.L., Russell, R.C., and Guan, K.-L. (2013). Amino acid signalling upstream of
837   mTOR. Nat. Rev. Mol. Cell Biol. *14*, 133–139. https://doi.org/10.1038/nrm3522.

838 Jiang, K., Rezabkova, L., Hua, S., Liu, Q., Capitani, G., Altelaar, A.F.M., Heck, A.J.R.,
839 Kammerer, R.A., Steinmetz, M.O., and Akhmanova, A. (2017). Microtubule minus-end
840 regulation at spindle poles by an ASPM-katanin complex. Nat. Cell Biol. *19*, 480–492.
841 https://doi.org/10.1038/ncb3511.

842 Kanton, S., Boyle, M.J., He, Z., Santel, M., Weigert, A., Sanchís-Calleja, F., Guijarro, P.,
843 Sidow, L., Fleck, J.S., Han, D., et al. (2019). Organoid single-cell genomic atlas uncovers
844 human-specific features of brain development. Nature *574*, 418–422.
845 https://doi.org/10.1038/s41586-019-1654-9.

846 Katsumoto, T., Aikawa, Y., Iwama, A., Ueda, S., Ichikawa, H., Ochiya, T., and
847 Kitabayashi, I. (2006). MOZ is essential for maintenance of hematopoietic stem cells.
848 Genes Dev. *20*, 1321–1330. https://doi.org/10.1101/gad.1393106.

849 Kilpinen, H., Goncalves, A., Leha, A., Afzal, V., Alasoo, K., Ashford, S., Bala, S.,
850 Bensaddek, D., Casale, F.P., Culley, O.J., et al. (2017). Common genetic variation drives
851 molecular heterogeneity in human iPSCs. Nature *546*, 370–375.
852 https://doi.org/10.1038/nature22403.

853 Kim, E., Novak, L.C., Lin, C., Colic, M., Bertolet, L.L., Gheorghe, V., Bristow, C.A.,
854 and Hart, T. (2022). Dynamic rewiring of biological activity across genotype and lineage
855 revealed by context-dependent functional interactions. Genome Biol. *23*, 140.
856 https://doi.org/10.1186/s13059-022-02712-z.

857 Kouprina, N., Pavlicek, A., Mochida, G.H., Solomon, G., Gersch, W., Yoon, Y.-H.,
858 Collura, R., Ruvolo, M., Barrett, J.C., Woods, C.G., et al. (2004). Accelerated evolution
859 of the ASPM gene controlling brain size begins prior to human brain expansion. PLoS
860 Biol. *2*, E126. https://doi.org/10.1371/journal.pbio.0020126.

861 Kreitzer, F.R., Salomonis, N., Sheehan, A., Huang, M., Park, J.S., Spindler, M.J.,
862 Lizarraga, P., Weiss, W.A., So, P.-L., and Conklin, B.R. (2013). A robust method to
863 derive functional neural crest cells from human pluripotent stem cells. Am. J. Stem Cells
864 *2*, 119–131. .

865 Kriegstein, A., Noctor, S., and Martínez-Cerdeño, V. (2006). Patterns of neural stem and
866 progenitor cell division may underlie evolutionary cortical expansion. Nat. Rev.
867 Neurosci. *7*, 883–890. https://doi.org/10.1038/nrn2008.

868 Kuhlwilm, M., and Boeckx, C. (2019). A catalog of single nucleotide changes
869 distinguishing modern humans from archaic hominins. Sci. Rep. *9*, 8463.
870 https://doi.org/10.1038/s41598-019-44877-x.

871 Lai, C.S., Fisher, S.E., Hurst, J.A., Vargha-Khadem, F., and Monaco, A.P. (2001). A
872 forkhead-domain gene is mutated in a severe speech and language disorder. Nature *413*,
873 519–523. https://doi.org/10.1038/35097076.

874   Lampert, E.J., Cimino-Mathews, A., Lee, J.S., Nair, J., Lee, M.-J., Yuno, A., An, D.,
875   Trepel, J.B., Ruppin, E., and Lee, J.-M. (2020). Clinical outcomes of prexasertib
876   monotherapy in recurrent BRCA wild-type high-grade serous ovarian cancer involve
877   innate and adaptive immune responses. J. Immunother. Cancer *8*, e000516.
878   https://doi.org/10.1136/jitc-2019-000516.

879   Lange, C., Huttner, W.B., and Calegari, F. (2009). Cdk4/CyclinD1 Overexpression in
880   Neural Stem Cells Shortens G1, Delays Neurogenesis, and Promotes the Generation and
881   Expansion of Basal Progenitors. Cell Stem Cell *5*, 320–331.
882   https://doi.org/10.1016/j.stem.2009.05.026.

883   Langergraber, K.E., Prüfer, K., Rowney, C., Boesch, C., Crockford, C., Fawcett, K.,
884   Inoue, E., Inoue-Muruyama, M., Mitani, J.C., Muller, M.N., et al. (2012). Generation
885   times in wild chimpanzees and gorillas suggest earlier divergence times in great ape and
886   human evolution. Proc. Natl. Acad. Sci. *109*, 15716–15721. .

887   Li, F., Kozono, D., Deraska, P., Branigan, T., Dunn, C., Zheng, X.-F., Parmar, K.,
888   Nguyen, H., DeCaprio, J., Shapiro, G.I., et al. (2020). CHK1 Inhibitor Blocks
889   Phosphorylation of FAM122A and Promotes Replication Stress. Mol. Cell *80*, 410-
890   422.e6. https://doi.org/10.1016/j.molcel.2020.10.008.

891   Li, W., Xu, H., Xiao, T., Cong, L., Love, M.I., Zhang, F., Irizarry, R.A., Liu, J.S., Brown,
892   M., and Liu, X.S. (2014). MAGeCK enables robust identification of essential genes from
893   genome-scale CRISPR/Cas9 knockout screens. Genome Biol. *15*, 554.
894   https://doi.org/10.1186/s13059-014-0554-4.

895   Lim, S., and Kaldis, P. (2012). Loss of Cdk2 and Cdk4 induces a switch from
896   proliferation to differentiation in neural stem cells. Stem Cells Dayt. Ohio *30*, 1509–
897   1520. https://doi.org/10.1002/stem.1114.

898   Liu, L., Michowski, W., Kolodziejczyk, A., and Sicinski, P. (2019a). The cell cycle in
899   stem cell proliferation, pluripotency and differentiation. Nat. Cell Biol. *21*, 1060–1067.
900   https://doi.org/10.1038/s41556-019-0384-4.

901   Liu, M.-H., Chen, J., Yang, Y.-S., Wang, Y.-Q., Chen, G.-Q., Zhang, Y., and Huang, Y.
902   (2021). FAM122A promotes acute myeloid leukemia cell growth through inhibiting
903   PP2A activity and sustaining MYC expression. Haematologica *106*, 903–907.
904   https://doi.org/10.3324/haematol.2020.251462.

905   Liu, S.J., Horlbeck, M.A., Cho, S.W., Birk, H.S., Malatesta, M., He, D., Attenello, F.J.,
906   Villalta, J.E., Cho, M.Y., Chen, Y., et al. (2017). CRISPRi-based genome-scale
907   identification of functional long noncoding RNA loci in human cells. Science *355*,
908   aah7111. https://doi.org/10.1126/science.aah7111.

909   Liu, X., Li, Y.I., and Pritchard, J.K. (2019b). Trans Effects on Gene Expression Can
910   Drive Omnigenic Inheritance. Cell *177*, 1022-1034.e6.
911   https://doi.org/10.1016/j.cell.2019.04.014.

912   Love, M.I., Huber, W., and Anders, S. (2014). Moderated estimation of fold change and
913   dispersion for RNA-seq data with DESeq2. Genome Biol. *15*, 550.
914   https://doi.org/10.1186/s13059-014-0550-8.

915   Lukaszewicz, A., Savatier, P., Cortay, V., Giroud, P., Huissoud, C., Berland, M.,
916   Kennedy, H., and Dehay, C. (2005). G1 phase regulation, area-specific cell cycle control,
917   and cytoarchitectonics in the primate cortex. Neuron *47*, 353–364.
918   https://doi.org/10.1016/j.neuron.2005.06.032.

919   Maguire, C.T., Demarest, B.L., Hill, J.T., Palmer, J.D., Brothman, A.R., Yost, H.J., and
920   Condic, M.L. (2013). Genome-Wide Analysis Reveals the Unique Stem Cell Identity of
921   Human Amniocytes. PLoS ONE *8*, e53372.
922   https://doi.org/10.1371/journal.pone.0053372.

923   Marchetto, M.C., Hrvoj-Mihic, B., Kerman, B.E., Yu, D.X., Vadodaria, K.C., Linker,
924   S.B., Narvaiza, I., Santos, R., Denli, A.M., Mendes, A.P., et al. (2019). Species-specific
925   maturation profiles of human, chimpanzee and bonobo neural cells. ELife *8*, e37527.
926   https://doi.org/10.7554/eLife.37527.

927   Marchetto, M.C.N., Narvaiza, I., Denli, A.M., Benner, C., Lazzarini, T.A., Nathanson,
928   J.L., Paquola, A.C.M., Desai, K.N., Herai, R.H., Weitzman, M.D., et al. (2013).
929   Differential L1 regulation in pluripotent stem cells of humans and apes. Nature *503*, 525–
930   529. https://doi.org/10.1038/nature12686.

931   McKenna, A., and Shendure, J. (2018). FlashFry: a fast and flexible tool for large-scale
932   CRISPR target design. BMC Biol. *16*, 74. https://doi.org/10.1186/s12915-018-0545-0.

933   Merkle, F.T., Ghosh, S., Kamitaki, N., Mitchell, J., Avior, Y., Mello, C., Kashin, S.,
934   Mekhoubad, S., Ilic, D., Charlton, M., et al. (2017). Human pluripotent stem cells
935   recurrently acquire and expand dominant negative P53 mutations. Nature *545*, 229–233.
936   https://doi.org/10.1038/nature22312.

937   Miller, J.R. (2001). The Wnts. Genome Biol. *3*, reviews3001.1.
938   https://doi.org/10.1186/gb-2001-3-1-reviews3001.

939   Mochida, S., Ikeo, S., Gannon, J., and Hunt, T. (2009). Regulated activity of PP2A-B55
940   delta is crucial for controlling entry into and exit from mitosis in Xenopus egg extracts.
941   EMBO J. *28*, 2777–2785. https://doi.org/10.1038/emboj.2009.238.

942   Mora-Bermúdez, F., Kanis, P., Macak, D., Peters, J., Naumann, R., Sarov, M., Winkler,
943   S., Oegema, C.E., Haffner, C., Xing, L., et al. (2022). Longer metaphase and fewer
944   chromosome segregation errors in modern human than Neandertal brain development.
945   2022.03.30.486431. https://doi.org/10.1101/2022.03.30.486431.

946   Muller, M.N., Wrangham, R.W., and Pilbeam, D.R. (2017). Chimpanzees and human
947   evolution.

948 Nonaka-Kinoshita, M., Reillo, I., Artegiani, B., Martínez-Martínez, M.Á., Nelson, M.,
949 Borrell, V., and Calegari, F. (2013). Regulation of cerebral cortex size and folding by
950 expansion of basal progenitors. EMBO J. *32*, 1817–1828.
951 https://doi.org/10.1038/emboj.2013.96.

952 Nüsslein-Volhard, C., and Wieschaus, E. (1980). Mutations affecting segment number
953 and polarity in Drosophila. Nature *287*, 795–801. https://doi.org/10.1038/287795a0.

954 Ortega, S., Prieto, I., Odajima, J., Martín, A., Dubus, P., Sotillo, R., Barbero, J.L.,
955 Malumbres, M., and Barbacid, M. (2003). Cyclin-dependent kinase 2 is essential for
956 meiosis but not for mitotic cell division in mice. Nat. Genet. *35*, 25–31.
957 https://doi.org/10.1038/ng1232.

958 Pacini, C., Dempster, J.M., Boyle, I., Gonçalves, E., Najgebauer, H., Karakoc, E., van der
959 Meer, D., Barthorpe, A., Lightfoot, H., Jaaks, P., et al. (2021). Integrated cross-study
960 datasets of genetic dependencies in cancer. Nat. Commun. *12*, 1661.
961 https://doi.org/10.1038/s41467-021-21898-7.

962 Pavlovic, B.J., Blake, L.E., Roux, J., Chavarria, C., and Gilad, Y. (2018). A Comparative
963 Assessment of Human and Chimpanzee iPSC-derived Cardiomyocytes with Primary
964 Heart Tissues. Sci. Rep. *8*, 15312. https://doi.org/10.1038/s41598-018-33478-9.

965 Peifer, M., and Wieschaus, E. (1990). The segment polarity gene armadillo encodes a
966 functionally modular protein that is the Drosophila homolog of human plakoglobin. Cell
967 *63*, 1167–1176. https://doi.org/10.1016/0092-8674(90)90413-9.

968 Pilaz, L.-J., Patti, D., Marcy, G., Ollier, E., Pfister, S., Douglas, R.J., Betizeau, M.,
969 Gautier, E., Cortay, V., Doerflinger, N., et al. (2009). Forced G1-phase reduction alters
970 mode of division, neuron number, and laminar phenotype in the cerebral cortex. Proc.
971 Natl. Acad. Sci. U. S. A. *106*, 21924–21929. https://doi.org/10.1073/pnas.0909894106.

972 Pollen, A.A., Bhaduri, A., Andrews, M.G., Nowakowski, T.J., Meyerson, O.S., Mostajo-
973 Radji, M.A., Di Lullo, E., Alvarado, B., Bedolli, M., Dougherty, M.L., et al. (2019).
974 Establishing Cerebral Organoids as Models of Human-Specific Brain Evolution. Cell
975 *176*, 743-756.e17. https://doi.org/10.1016/j.cell.2019.01.017.

976 Pontis, J., Planet, E., Offner, S., Turelli, P., Duc, J., Coudray, A., Theunissen, T.W.,
977 Jaenisch, R., and Trono, D. (2019). Hominoid-Specific Transposable Elements and
978 KZFPs Facilitate Human Embryonic Genome Activation and Control Transcription in
979 Naive Human ESCs. Cell Stem Cell *24*, 724-735.e5.
980 https://doi.org/10.1016/j.stem.2019.03.012.

981 Prado-Martinez, J., Sudmant, P.H., Kidd, J.M., Li, H., Kelley, J.L., Lorente-Galdos, B.,
982 Veeramah, K.R., Woerner, A.E., O'Connor, T.D., Santpere, G., et al. (2013). Great ape
983 genetic diversity and population history. Nature *499*, 471–475.
984 https://doi.org/10.1038/nature12228.

30

985   Prescott, S.L., Srinivasan, R., Marchetto, M.C., Grishina, I., Narvaiza, I., Selleri, L.,
986   Gage, F.H., Swigut, T., and Wysocka, J. (2015). Enhancer Divergence and cis-
987   Regulatory Evolution in the Human and Chimp Neural Crest. Cell *163*, 68–83.
988   https://doi.org/10.1016/j.cell.2015.08.036.

989   Rakic, P. (1995). A small step for the cell, a giant leap for mankind: a hypothesis of
990   neocortical expansion during evolution. Trends Neurosci. *18*, 383–388.
991   https://doi.org/10.1016/0166-2236(95)93934-p.

992   Rubin, S.M., Sage, J., and Skotheim, J.M. (2020). Integrating Old and New Paradigms of
993   G1/S Control. Mol. Cell *80*, 183–192. https://doi.org/10.1016/j.molcel.2020.08.020.

994   Ryu, H., Inoue, F., Whalen, S., Williams, A., Kircher, M., Martin, B., Alvarado, B.,
995   Samee, Md.A.H., Keough, K., Thomas, S., et al. (2018). Massively parallel dissection of
996   human accelerated regions in human and chimpanzee neural progenitors. BioRxiv
997   256313. https://doi.org/10.1101/256313.

998   Sanjana, N.E., Shalem, O., and Zhang, F. (2014). Improved vectors and genome-wide
999   libraries for CRISPR screening. Nat. Methods *11*, 783–784.
1000   https://doi.org/10.1038/nmeth.3047.

1001   Satyanarayana, A., and Kaldis, P. (2009). Mammalian cell-cycle regulation: several
1002   Cdks, numerous cyclins and diverse compensatory mechanisms. Oncogene *28*, 2925–
1003   2939. https://doi.org/10.1038/onc.2009.170.

1004   Serin Harmanci, A., Harmanci, A.O., and Zhou, X. (2020). CaSpER identifies and
1005   visualizes CNV events by integrative analysis of single-cell or bulk RNA-sequencing
1006   data. Nat. Commun. *11*, 89. https://doi.org/10.1038/s41467-019-13779-x.

1007   Setoguchi, K., TeSlaa, T., Koehler, C.M., and Teitell, M.A. (2016). P53 Regulates Rapid
1008   Apoptosis in Human Pluripotent Stem Cells. J. Mol. Biol. *428*, 1465–1475.
1009   https://doi.org/10.1016/j.jmb.2015.07.019.

1010   Shirodkar, S., Ewen, M., DeCaprio, J.A., Morgan, J., Livingston, D.M., and Chittenden,
1011   T. (1992). The transcription factor E2F interacts with the retinoblastoma product and a
1012   p107-cyclin A complex in a cell cycle-regulated manner. Cell *68*, 157–166.
1013   https://doi.org/10.1016/0092-8674(92)90214-w.

1014   Suzuki, I.K., Gacquer, D., Van Heurck, R., Kumar, D., Wojno, M., Bilheu, A., Herpoel,
1015   A., Lambert, N., Cheron, J., Polleux, F., et al. (2018). Human-Specific NOTCH2NL
1016   Genes Expand Cortical Neurogenesis through Delta/Notch Regulation. Cell *173*, 1370-
1017   1384.e16. https://doi.org/10.1016/j.cell.2018.03.067.

1018   Szklarczyk, D., Gable, A.L., Nastou, K.C., Lyon, D., Kirsch, R., Pyysalo, S., Doncheva,
1019   N.T., Legeay, M., Fang, T., Bork, P., et al. (2021). The STRING database in 2021:
1020   customizable protein–protein networks, and functional characterization of user-uploaded

31

1021   gene/measurement sets. Nucleic Acids Res. *49*, D605–D612.
1022   https://doi.org/10.1093/nar/gkaa1074.

1023   Taverna, E., Götz, M., and Huttner, W.B. (2014). The cell biology of neurogenesis:
1024   toward an understanding of the development and evolution of the neocortex. Annu. Rev.
1025   Cell Dev. Biol. *30*, 465–502. https://doi.org/10.1146/annurev-cellbio-101011-155801.

1026   Thomson, J.A., Itskovitz-Eldor, J., Shapiro, S.S., Waknitz, M.A., Swiergiel, J.J.,
1027   Marshall, V.S., and Jones, J.M. (1998). Embryonic stem cell lines derived from human
1028   blastocysts. Science *282*, 1145–1147. https://doi.org/10.1126/science.282.5391.1145.

1029   Tian, R., Gachechiladze, M.A., Ludwig, C.H., Laurie, M.T., Hong, J.Y., Nathaniel, D.,
1030   Prabhu, A.V., Fernandopulle, M.S., Patel, R., Abshari, M., et al. (2019). CRISPR
1031   Interference-Based Platform for Multimodal Genetic Screens in Human iPSC-Derived
1032   Neurons. Neuron *104*, 239-255.e12. https://doi.org/10.1016/j.neuron.2019.07.014.

1033   Tsherniak, A., Vazquez, F., Montgomery, P.G., Weir, B.A., Kryukov, G., Cowley, G.S.,
1034   Gill, S., Harrington, W.F., Pantel, S., Krill-Burger, J.M., et al. (2017). Defining a Cancer
1035   Dependency Map. Cell *170*, 564-576.e16. https://doi.org/10.1016/j.cell.2017.06.010.

1036   Ullah, M., Pelletier, N., Xiao, L., Zhao, S.P., Wang, K., Degerny, C., Tahmasebi, S.,
1037   Cayrou, C., Doyon, Y., Goh, S.-L., et al. (2008). Molecular architecture of quartet
1038   MOZ/MORF histone acetyltransferase complexes. Mol. Cell. Biol. *28*, 6828–6843.
1039   https://doi.org/10.1128/MCB.01297-08.

1040   Varki, A., and Altheide, T.K. (2005). Comparing the human and chimpanzee genomes:
1041   Searching for needles in a haystack. Genome Res. *15*, 1746–1758.
1042   https://doi.org/10.1101/gr.3737405.

1043   Vassilev, L.T., Vu, B.T., Graves, B., Carvajal, D., Podlaski, F., Filipovic, Z., Kong, N.,
1044   Kammlott, U., Lukacs, C., Klein, C., et al. (2004). In vivo activation of the p53 pathway
1045   by small-molecule antagonists of MDM2. Science *303*, 844–848.
1046   https://doi.org/10.1126/science.1092472.

1047   Wainberg, M., Kamber, R.A., Balsubramani, A., Meyers, R.M., Sinnott-Armstrong, N.,
1048   Hornburg, D., Jiang, L., Chan, J., Jian, R., Gu, M., et al. (2021). A genome-wide atlas of
1049   co-essential modules assigns function to uncharacterized genes. Nat. Genet. *53*, 638–649.
1050   https://doi.org/10.1038/s41588-021-00840-z.

1051   Wang, L., Wu, D., Robinson, C.V., Wu, H., and Fu, T.-M. (2020). Structures of a
1052   Complete Human V-ATPase Reveal Mechanisms of Its Assembly. Mol. Cell *80*, 501-
1053   511.e3. https://doi.org/10.1016/j.molcel.2020.09.029.

1054   Wang, T., Wei, J.J., Sabatini, D.M., and Lander, E.S. (2014). Genetic screens in human
1055   cells using the CRISPR-Cas9 system. Science *343*, 80–84.
1056   https://doi.org/10.1126/science.1246981.

1057 Weinstein, J.N., Collisson, E.A., Mills, G.B., Shaw, K.M., Ozenberger, B.A., Ellrott, K.,
1058 Shmulevich, I., Sander, C., and Stuart, J.M. (2013). The Cancer Genome Atlas Pan-
1059 Cancer Analysis Project. Nat. Genet. *45*, 1113–1120. https://doi.org/10.1038/ng.2764.

1060 White, J.K., Gerdin, A.-K., Karp, N.A., Ryder, E., Buljan, M., Bussell, J.N., Salisbury, J.,
1061 Clare, S., Ingham, N.J., Podrini, C., et al. (2013). Genome-wide Generation and
1062 Systematic Phenotyping of Knockout Mice Reveals New Roles for Many Genes. Cell
1063 *154*, 452–464. https://doi.org/10.1016/j.cell.2013.06.022.

1064 Wieschaus, E., and Nüsslein-Volhard, C. (2016). The Heidelberg Screen for Pattern
1065 Mutants of Drosophila: A Personal Account. Annu. Rev. Cell Dev. Biol. *32*, 1–46.
1066 https://doi.org/10.1146/annurev-cellbio-113015-023138.

1067 Yang, X.-J. (2015). MOZ and MORF acetyltransferases: Molecular interaction, animal
1068 development and human disease. Biochim. Biophys. Acta BBA - Mol. Cell Res. *1853*,
1069 1818–1826. https://doi.org/10.1016/j.bbamcr.2015.04.014.

1070 Zatulovskiy, E., Zhang, S., Berenson, D.F., Topacio, B.R., and Skotheim, J.M. (2020).
1071 Cell growth dilutes the cell cycle inhibitor Rb to trigger cell division. Science *369*, 466–
1072 471. https://doi.org/10.1126/science.aaz6213.

1073 Zhang, J. (2003). Evolution of the human ASPM gene, a major determinant of brain size.
1074 Genetics *165*, 2063–2070. https://doi.org/10.1093/genetics/165.4.2063.

1075 Zhou, J., Su, P., Wang, L., Chen, J., Zimmermann, M., Genbacev, O., Afonja, O., Horne,
1076 M.C., Tanaka, T., Duan, E., et al. (2009). mTOR supports long-term self-renewal and
1077 suppresses mesoderm and endoderm activities of human embryonic stem cells. Proc.
1078 Natl. Acad. Sci. *106*, 7840–7845. https://doi.org/10.1073/pnas.0901854106.

1079 Zhou, Y., Shi, W.-Y., He, W., Yan, Z.-W., Liu, M.-H., Chen, J., Yang, Y.-S., Wang, Y.-
1080 Q., Chen, G.-Q., and Huang, Y. (2020). FAM122A supports the growth of hepatocellular
1081 carcinoma cells and its deletion enhances Doxorubicin-induced cytotoxicity. Exp. Cell
1082 Res. *387*, 111714. https://doi.org/10.1016/j.yexcr.2019.111714.

1083 Zhu, L., Harlow, E., and Dynlacht, B.D. (1995). p107 uses a p21CIP1-related domain to
1084 bind cyclin/cdk2 and regulate interactions with E2F. Genes Dev. *9*, 1740–1752.
1085 https://doi.org/10.1101/gad.9.14.1740.

1086 Zoncu, R., Bar-Peled, L., Efeyan, A., Wang, S., Sancak, Y., and Sabatini, D.M. (2011).
1087 mTORC1 Senses Lysosomal Amino Acids Through an Inside-Out Mechanism That
1088 Requires the Vacuolar H+-ATPase. Science *334*, 678–683.
1089 https://doi.org/10.1126/science.1207056.

1090

STAR METHODS

KEY RESOURCES TABLE

REAGENT or RESOURCE	Source	Identifier
Antibodies		
anti-pS6, rabbit, 1:1,000	Cell Signaling	Cat# 2211S; RRID: AB_331679
anti-GAPDH, rabbit, 1:1,000	Proteintech	Cat# 10494-1-AP; RRID: AB_2263076
anti-PAX6, human, 1:50	Miltenyi	Cat# 130-123-328; RRID: AB_2819477
anti-B2M, mouse, 1:20	BioLegend	Cat# 316312; RRID: AB_10641281
anti-Nestin, mouse, 1:20	BioLegend	Cat# 656805; RRID: AB_2566381
Goat anti-Rabbit IGG secondary IRDye 680RD, 1:15,000	LI-COR	Cat# 926-68071; RRID: AB_10956166
Goat anti-Rabbit IGG secondary IRDye 800CW, 1:15,000	LI-COR	Cat# 926-32211; RRID: AB_621843
Bacterial and virus strains		
MegaX Competent Cells	ThermoFisher	Cat# C640003
Stellar Competent Cells	Takara	Cat# 636766
Chemicals, peptides, and recombinant proteins		
TransIT-LT1 Transfection Reagent	Mirus Bio	Cat# MIR2300
Lipofectamine Stem Transfection Reagent	ThermoFisher	Cat# STEM00008
SB431542	Miltenyi	Cat# 130-106-543
Noggin	Miltenyi	Cat# 130-103-456
ROCK inhibitor thiazovivin	Stem Cell Tech.	72252
Puromycin	Goldbio	P-600-100
Chroman 1	Tocris	Cat# 7163
Emricasan	Selleck Chemicals	Cat# S7775
Polyamine Supplement	Sigma	Cat# P8483
Trans-ISRIB	Tocris	Cat# 5284
Critical commercial assays		
Macherey-Nagel NucleoSpin Blood XL	ThermoFisher	Cat# NC1105387
Superscript IV VILO	ThermoFisher	Cat# 11756050
DyNAmo ColorFlash SYBR Green	ThermoFisher	Cat# F416L
Click-iT Plus EdU Alexa Fluor 647 Flow Cytometry Assay	ThermoFisher	Cat# C10635
BD Cytofix/Cytoperm	ThermoFisher	Cat# BDB554714
Deposited Data		
Raw sequencing data from bulk RNA-seq	This paper	GEO
Processed sequencing data from bulk RNA-seq	This paper	Table S2
Experimental Models: Cell lines		
Chimpanzee iPSC 3624K dCas9-KRAB-mCherry	This paper	N/A

Chimpanzee iPSC 3624K dCas9-KRAB-BFP	This paper	N/A
Chimpanzee iPSC 3649 dCas9-KRAB-BFP	This paper	N/A
Chimpanzee iPSC 40290F dCas9-KRAB-mCherry	This paper	N/A
Chimpanzee iPSC 8861G dCas9-KRAB-mCherry	This paper	N/A
Chimpanzee iPSC 8861G dCas9-KRAB-BFP	This paper	N/A
Chimpanzee iPSC Pt-5c dCas9-KRAB-BFP	This paper	N/A
Human iPSC 20961B dCas9-KRAB-BFP	This paper	N/A
Human iPSC 20961B dCas9-KRAB-GFP	This paper	N/A
Human iPSC 21792A dCas9-KRAB-BFP	This paper	N/A
Human iPSC 23555A dCas9-KRAB-BFP	This paper	N/A
Human iPSC 23555A dCas9-KRAB-GFP	This paper	N/A
Human iPSC 28128B dCas9-KRAB-BFP	This paper	N/A
Human iPSC 28128B dCas9-KRAB-GFP	This paper	N/A
Human ESC H1 dCas9-KRAB-BFP	This paper	N/A
Human iPSC WTC11 dCas9-KRAB-BFP	This paper	N/A
Oligonucleotides		
See Table S6 for oligonucleotides used in this study	This paper	N/A
Recombinant DNA		
pX458	Addgene	Cat# 48138
Gen3-AAVS1 dCas9-XTEN-KRAB-P2A-BFP	Addgene	Cat# 127968
pEF1-BCL-XL	(Li et al., 2018)	
pCRISPRia-v2	Addgene (Adamson et al., 2016)	Cat# #84832
Software and Algorithms		
CRISPRi screen processing for sgRNA counts	(Horlbeck et al., 2016)	https://github.com/mhorlbeck/ScreenProcessing
MaGeCK	(Li et al., 2014)	https://sourceforge.net/projects/mageck/
FlashFry	(McKenna and Shendure, 2018)	https://github.com/mckennalab/FlashFry
Cutadapt	(Martin, 2011)	https://cutadapt.readthedocs.io/en/stable/
kallisto	(Bray et al., 2016)	https://pachterlab.github.io/kallisto/
gffread	(Pertea and Pertea, 2020)	https://github.com/gpertea/gffread
tximport	(Soneson et al., 2015)	https://bioconductor.org/packages/release/bioc/html/tximport.html
DESeq2	(Love et al., 2014)	https://bioconductor.org/packages/release/bioc/html/DESeq2.html

CONTACT FOR REAGENT AND RESOURCE SHARING

Further information and requests for resources and reagents should be directed to and will be fulfilled by the Lead Contact, Alex A Pollen (Alex.Pollen@ucsf.edu).

Cell Lines
All cell lines used in this study are listed in Supplementary Table 1.

Primers
All primers used in this study are listed in Supplementary Table 6.

Media Formulations
mTESR1 was purchased from Stem Cell Technologies (cat. 85850) and supplemented with 100 units/ml penicillin, 100 µg/ml streptomycin, and 292 µg/ml L-glutamine (Gibco, cat. 10378016). StemFlex was purchased from Gibco (cat. A3349401) and supplemented with 100 units/ml penicillin, 100 µg/ml streptomycin, and 292 µg/ml L-glutamine. HEK293Ts were cultured in DMEM (ThermoFisher, cat. 11965118) supplemented with 10% FBS (VWR, cat. 97068-085, lot 043K20), 100 units/ml penicillin, 100 µg/ml streptomycin, and 292 µg/ml L-glutamine. Neuronal differentiation media was prepared as described in (Nolbrant et al., 2017), with DMEM F/12 (ThermoFisher, cat. 21331020), CTS Neurobasal Medium (ThermoFisher, cat. A1371201), 1x N-2 supplement CTS (ThermoFisher, cat. A1370701), 10 µM SB431542 (StemMACS, TGFβ inhibitor; Miltenyi, cat. 130-106-543), 100 ng/ml Noggin (recombinant human; Miltenyi, cat. 130-103-456), and 100 units/ml penicillin, 100 µg/ml streptomycin, and 292 µg/ml L-glutamine. Thiazovivin (Stem Cell Technologies, cat. 72252) was included at a concentration of 2 µM during passaging. For single cell sorting and lipofection, we used the CEPT cocktail (Chen et al., 2021) consisting of 50 nM chroman 1 (Tocris Bioscience, cat. 7163), 5 µM emricasan (Selleck Chemicals, cat. S7775), polyamine supplement diluted 1:1,000 (Sigma-Aldrich, cat. P8483), and 0.7 µM trans-ISRIB (Tocris Bioscience, cat. 5284).

Construction of CRISPRi cell lines
All wildtype cell lines tested negative for mycoplasma prior to the start of cell line engineering. The CRISPRi effector protein dCas9-KRAB was introduced into either the CLYBL or AAVS1 safe harbor locus (Cheung et al., 1980; Hockemeyer et al., 2009; Philpott et al., 2002; Smith et al., 2008) via lipofection of three plasmids: 1) A modified version of pX458 (Addgene #48138), containing both Cas9 nuclease and a sgRNA targeting either CLYBL or AAVS1. The sgRNA spacer was modified from the original plasmid by cutting with type IIS restriction endonuclease BbsI-HF. Complementary oligos containing the sgRNA spacer and proper overhangs were annealed and ligated with T4 ligase. 2) A modified version of the Gen3-AAVS1 vector from (Mandegar et al., 2016) containing dCas9-XTEN-KRAB-P2A-BFP driven by the chicken beta-actin (CAG) promoter, flanked by homology arms to CLYBL (Addgene #127968) or AAVS1. 3) pEF1-BCL-XL, a plasmid expressing BCL-XL, the anti-apoptotic isoform of BCL2L1, from the EF-1a promoter. Lipofection was performed as follows: two days prior to transfection, cells were switched into mTESR1 media on a non-passaging day. One day prior to transfection, ~400,000 cells were plated into a Matrigel-coated (Corning, cat. 354230) 6-well plate with mTESR1 supplemented with 2 µM thiazovivin. On the day of transfection, a 3 µg mixture of plasmids 1-3 was made at a mass ratio of 5:5:1, added to a mixture of 96 µl Opti-MEM (Gibco, cat. 31985062) and 4 µl Lipofectamine Stem (ThermoFisher, cat. STEM00003), and incubated at room

temperature for 10 minutes. Media was aspirated from the PSC plate and replaced with 2 ml Opti-MEM supplemented with CEPT. The lipid/plasmid DNA complexes were then added to plate and incubated for 4 hours, after which 2 ml of mTESR1 supplemented with CEPT was overlaid. 24 hr post-transfection, media was replaced with StemFlex supplemented with CEPT. 48 hr post-transfection, media was replaced with StemFlex supplemented with 2 µM thiazovivin, and cells were then passaged for 10-14 days to dilute out the transfected plasmids. Single cell clones and one polyclonal population per cell line were then sorted on a Sony MA900 (see Table S1). Expanded populations were cryopreserved in Bambanker preservation media (ThermoFisher, cat. 50999554) and functionally validated with an sgRNA targeting B2M, a non-essential surface marker. B2M levels were measured by staining with an APC anti-human β2-microglobulin antibody (BioLegend, cat. 316312).

Lentivirus production, concentration, and titration
Lentivirus for CRISPRi screening was produced in HEK293T cells. HEK293Ts were seeded at a density of 80,000 cells/cm^2 24 hr. prior to transfection in 15 cm dishes. Next, each dish was transduced with 20 µg sgRNA library, 6.75 µg standard lentivirus packaging vectors, and 81 µl Mirus transfection reagent (VWR, cat. 10767-122) in Opti-MEM. 24 hr. post-transfection, media was replaced and supplemented with 1X ViralBoost (Alstem, cat. VB100). Supernatant was collected at 48 hr. post-transfection and concentrated 1:10 with Lenti-X Concentrator (Takara Bio, cat. 631231). Concentrated lentivirus was titered in PSCs based on BFP expression 3 days post-infection using a flow cytometer.

Pooled genome-wide CRISPRi screening
CRISPRi PSCs expressing dCas9-KRAB were dissociated with Accutase (Innovative Cell Technologies, cat. AT104-500), resuspended in StemFlex supplemented with 2 µM thiazovivin and 5 µg/ml polybrene (Sigma-Aldrich, cat. TR-1003-G), transduced with the lentiviral hCRISPRi-v2 sgRNA library at a target infection rate of 25-40%, and plated in Matrigel-coated 5-layer cell culture flasks (Corning, cat. 353144) at a density of 65,000-80,000 cells/cm^2. The following day, StemFlex medium was replaced. Two days after infection, cells were dissociated with Accutase, resuspended in StemFlex supplemented with 2 µM thiazovivin and 1.5 µg/ml puromycin (Goldbio, cat. P-600-100), and plated in 5-layer cell culture flasks. The following day, medium was replaced with StemFlex supplemented with 1.5 µg/ml puromycin. Four days after infection, 100 M cells were harvested for the initial time point (t_0), while 250-300 M cells were resuspended in StemFlex supplemented with 1.5 µg/ml puromycin and plated in 5-layer cell culture flasks (>1000x sgRNA library representation). Selection efficiency was assessed by flow cytometry (>70% BFP+). Every two days, cells were dissociated with Accutase, resuspended in StemFlex supplemented with 2 µM thiazovivin, and plated at a density of 80,000-100,000 cells/cm^2. Technical replicates were cultured separately for the duration of the screen. After 10 days of growth, 150 M cells from each technical replicate were harvested for the final time point (t_{final}). Genomic DNA was isolated from frozen cell pellets using the Macherey-Nagel NucleoSpin Blood XL kit (Macherey-Nagel). Isolated DNA was quantified using a NanoDrop (ThermoFisher) and the sgRNA expression cassette was amplified by 22 cycles of PCR using NEBNext Ultra II Q5 Master Mix (NEB) and primers containing Illumina P5/P7 termini and sample-specific TruSeq indices. Each sample was distributed into 150-200 individual 100 µl reactions in 96-well plates, each with 10 µg genomic DNA as input. Following amplification, reactions from each sample were pooled and a 100 µl aliquot was purified using AMPure XP beads (Beckman-Coulter) with a two-

sided size selection. Purified libraries were quantified using a Qubit (ThermoFisher) and sequenced using an Illumina HiSeq 4000 (SE50, 5% PhiX) with a custom sequencing primer (oCRISPRi_seq V5).

Data analysis for pooled genome-wide CRISPRi screens

Sequencing data were aligned to hCRISPRi-v2 and quantified using the ScreenProcessing pipeline (https://github.com/mhorlbeck/ScreenProcessing) (Horlbeck et al., 2016). sgRNA counts were then processed using MAGeCK (Li et al., 2014) test (--norm-method control --remove-zero control --gene-test-fdr-threshold 0.10 --remove-zero-threshold 50 --gene-lfc-method alphamean) and separately using a custom analysis method inspired by MAGeCK. Briefly, sgRNA counts were normalized by the median ratio method. Mean-variance modeling was performed with non-targeting sgRNAs as the control group, and sample mean and variance values were used to parameterize a negative binomial distribution. *P*-values were then calculated for each sgRNA based on the tail probability of the negative binomial and *P*-value cut-offs were chosen such that 95% of non-targeting sgRNAs were not significant.

For each gene, sgRNAs were filtered by two criteria: 1) perfect alignment to both the human (hg38) and chimpanzee (panTro6) reference genomes, as determined by FlashFry (McKenna and Shendure, 2018), and 2) significance according to the negative binomial distribution. Only sgRNAs passing both filters were retained for analysis, resulting in a variable number of sgRNAs per gene (0-5 sgRNAs). The remaining sgRNA counts were converted to $\log_2$ fold-change and averaged to produce a gene score. Significance testing for gene scores was performed by bootstrapping non-targeting sgRNAs, with groups of 1-5 random non-targeting sgRNAs assigned to each control gene to select candidates from the initial genome-wide screens.

Essential genes for each screen (Fig. 1B) were determined by the degree of depletion among sgRNAs targeting the gene. To facilitate equal comparison among screens, the top 3000 most depleted genes in each screen were defined as essential (with mean sgRNA depletion greater than 4-fold for all such genes). In addition, genes with mean sgRNA depletion less than 2-fold were defined as non-essential. Each intersection set was then constructed based on two inclusion criteria: genes were required to be essential for each member of the set and non-essential for all non-members of the set.

For comparison of technical replicates (Fig. 1B), identification of shared essential genes (Fig. 1B), and assessment of screen performance using DepMap Public 21Q4 gene sets (Fig. 1C), all hCRISPRi-v2 sgRNAs, including those with mismatched targets in the panTro6 reference genome, were included for analysis. Mismatches specific to each individual cell line were not considered, as high-quality genome sequences of each cell line were not available. However, these mismatches should in theory affect only a small fraction of all sgRNAs. For identification of candidate genes with species-specific effects on proliferation (Fig. 1D), only sgRNAs with perfect-match targets in the panTro6 reference genome (77.4%, $n = 79417/102640$) and transcriptional start sites targeted by at least three sgRNAs after excluding mismatched sgRNAs (86.7%, $n = 17804/20528$), were retained for analysis.

For screen analysis using MAGeCK, genes with false discovery rates (FDRs) less than 10% for both individuals within a species and FDRs greater than 25% in both individuals from the opposite species were considered as candidates for validation screening ($n = 418$ genes).

CEV-v1 validation screening library design

To validate genome-wide screens, a Comparative Essential Validation (CEV-v1) sgRNA library consisting of 9,692 sgRNAs targeting 963 candidate species-specific essential or proliferation suppressor genes was constructed. hCRISPRi-v2 sgRNAs with perfect-match targets in panTro6 exhibiting significant depletion or enrichment in the genome-wide screens were retained in CEV-v1 ($n = 3589$ sgRNAs). In addition, new sgRNAs with perfect-match target sites in the human (hg38) and chimpanzee (panTro6) reference genomes were chosen based on their position relative to the FANTOM-annotated transcriptional start site (Horlbeck et al., 2016) on-target activity predicted by DeepHF (Wang et al., 2019), and off-target potential predicted by a genome-wide search of mismatched target sites (Jost et al., 2020; McKenna and Shendure, 2018) in both reference genomes. Briefly, after performing off-target filtering (one perfect-match target, CRISPRi specificity score > 0.20, maximal predicted activity at any off-target site < 0.80), candidate sgRNAs were categorized by their position relative to the FANTOM TSS and then ranked by their DeepHF score. A threshold DeepHF score was imposed by excluding sgRNAs with predicted activities less than one standard deviation below the mean of all candidate sgRNAs (minimum score: 0.4378). Eight sgRNAs were selected for each gene as well as 1845 non-targeting sgRNAs from hCRISPRi-v2. Oligonucleotide pools were designed with flanking PCR and restriction sites (BstXI, BlpI), synthesized by Agilent Technologies, and cloned into the sgRNA expression vector pCRISPRia-v2 (Addgene #84832) as described previously (Gilbert et al., 2014).

Pooled validation CRISPRi screening

Validation screens were performed in conditions consistent with the genome-wide screens. Briefly, CRISPRi PSCs expressing dCas9-KRAB were dissociated with Accutase, resuspended in StemFlex supplemented with 2 µM thiazovivin and 5 µg/ml polybrene, transduced with the lentiviral CEV-v1 sgRNA library at a target infection rate of 25-40%, and plated in Matrigel-coated 3-layer cell culture flasks (Corning, cat. 353143) at a density of 65,000-80,000 cells/cm^2. Cells were dissociated, plated, selected with puromycin, and grown on the same schedule as used for the genome-wide screens. Technical replicates were cultured separately for the duration of the screen and >1000x sgRNA library representation was maintained. For individuals screened twice (H20961B, H23555A, H28126B, C3624K, C8861G), replicate screens were performed independently at the Whitehead Institute and UCSF.

Data analysis for CEV-v1 validation screens

Sequencing data were aligned to CEV-v1 and quantified using the ScreenProcessing pipeline and MAGeCK. A matrix containing sgRNA counts from all CEV-v1 screens (excluding C3649 and Pt5-C due to non-responsiveness to $MDM2/p53$ perturbations) was assembled and used as input for differential analysis by DESeq2. Briefly, each sample was annotated by species, individual, and timepoint and a design matrix was created to model the species-specific effect of time (t_0 vs. t_{final}) while controlling for individual effects (modeled as fixed effects) within each species. The human and chimpanzee species terms were then contrasted to extract a Benjamini–Hochberg-adjusted P-value and $\log_2$ fold-change for each sgRNA. sgRNA adjusted P-values were combined into gene FDRs using alpha-robust rank aggregation (α-RRA) from MAGeCK and the α threshold

(to remove the effect of insignificant sgRNAs from the assessment of gene significance) was set according to the fraction of sgRNAs with an adjusted P-value < 0.01. For each gene, $\log_2$ fold-change was computed as the mean of the four sgRNAs with the largest absolute fold-change. To exclude genes with shared effects from being erroneously called as species-specific, any gene with an FDR in both the human and chimpanzee species terms less than the highest FDR for any gene with at least one sgRNA passing the α threshold in α-RRA was discarded. For each gene in the set of 75 genes with species-specific effects reported in Fig. 2, we required that three conditions be met in the chimpanzee–human contrast term: (1) gene FDR < 0.01, (2) at least three sgRNAs targeting the gene pass the α threshold in α-RRA, and (3) gene $\log_2$ fold-change difference ≥ 0.75 between species. We used the STRING database v11.5 (Szklarczyk et al., 2021) to identify known and predicted protein–protein interactions among this set of 75 genes.

To quantify sources of variation in CEV-v1 screens, a matrix of sgRNA counts was assembled as described above and normalized using edgeR (Robinson et al., 2010) calcNormFactors. Normalized sgRNA counts were then prepared for linear modeling using variancePartition voomWithDreamWeights and a linear mixed model was fit using variancePartition fitExtractVarPartModel. The categorical variables species, individual, and timepoint were modeled as random effects. For each gene (Fig. S2B), gene-level estimates of variance were determined by computing the mean variance attributable to each variable for all sgRNAs targeting that gene.

Quantitative RT-PCR
Biological triplicates were grown in a 6-well plate and infected with sgRNAs (see Table S2) at an MOI of ~0.3. 48h post-infection, cells were expanded in 2 µg/ml puromycin and allowed to recover for 48 hours. At day 5 post-infection, sgRNA+ cells were sorted to purity based on BFP+ expression on a Sony MA900 cell sorter. Cells were then allowed to recover for 48-96 hours, until they reached ~60-80% confluence on a 6-well plate. RNA was extracted with a Direct-zol RNA miniprep kit (Zymo Research, cat. R2051). RNA was reverse transcribed with SuperScript IV VILO (ThermoFisher, cat. 11756050), and cDNA was amplified with the DyNAmo ColorFlash SYBR Green kit (ThermoFisher, cat. F416L). Primers for GAPDH were used as loading controls and no-RT controls were performed to control for genomic DNA contamination. Amplifications were performed in duplicate and quantified on a QuantStudio Flex 7 Real-Time PCR system in 96-well plates.

Copy number variation analysis
Chromosomal copy number variations (CNV) were inferred with the InferCNV R package (version 1.2.1), which predicts CNVs based on gene expression data. InferCNV was run in 'subclusters' analysis mode using 'random_trees' as the subclustering method with gene expression quantified for both species by alignment to the hg38 reference genome. Average gene expression across all six individuals in each species was used as the background column. The cut-off for the minimum average read count per gene among reference cells was set to 1, per software recommendation for bulk RNA-seq data. CNV prediction was performed with the 'i6' Hidden Markov Model, whose output CNV states were filtered with the included Bayesian mixture model with a threshold of 0.1 to find the most confident CNVs. All other options were set to their default values.

To check for copy number variation at a selected set of cell cycle-related genes, we analyzed whole-genome shotgun sequencing data. Genomic DNA from all libraries sequenced on an Illumina sequencer in 151 bp paired-end mode was provided for analysis courtesy of the laboratory of Gregory Wray and mapped to chimpanzee reference panTro6 (Kronenberg et al., 2018) using bwa-mem2 (https://ieeexplore.ieee.org/document/8820962) with default parameters. PicardTools (https://broadinstitute.github.io/picard) was used to add read group information and mark duplicates, and baseline coverage histograms were generated using BEDTools genomecov (Quinlan and Hall, 2010), from which the 5th, 50th, and 95th percentile of coverage for each library, both genome-wide and across chromosome X, were extracted. Gene-level features for all genes listed as cyclins, cyclin dependent kinases, and class III Cys-based CDC25 phosphatases in the HGNC database (Tweedie et al., 2021) were selected from a recent chimpanzee gene annotation (Mao et al., 2021) and the coverage at each base across the full length of each gene in the set for each library was counted and summed using samtools mpileup (Li et al., 2009). For this step, only primary alignments containing mapped reads not marked as duplicates, with minimum map quality of 20, were considered (samtools view -F1284 -q20).

RNA-seq library prep and analysis

Human (WTC11) and chimpanzee (C3649) cells were infected with individual sgRNAs targeting KAT6A or BRPF1. Cells were expanded for 5 days. At day 5, ~1M sgRNA expressing cells were sorted on a Sony MA900 cell sorter based on BFP+ expression. Cells were then pelleted, snap-frozen and stored at -80°C. High quality RNA was extracted by adding RNAse-free Trizol (ThermoFisher, cat. 15596026) to each pellet and processing with the Zymo Research Direct-zol RNA miniprep kit (Zymo Research, cat. R2050). RNA-seq was performed using the Illumina TruSeq Stranded Total RNA kit (Illumina, cat. 20020599) according to the manufacturer's instructions, with the exception of the final PCR step for which only 10 cycles were used to prevent overamplification. The final pooled library was sequenced with 50 bp single end reads on a HiSeq 2500.

Raw bulk RNA-seq reads from knockdown experiments and wild-type chimpanzee and human iPSCs were adapter-trimmed using cutadapt (Martin, 2011) (with option -b AGATCGGAAGAGCACACGTCTGAACTCCAGTCA) and then pseudo-aligned to species-specific transcriptomes using kallisto (Bray et al., 2016) with options --single -l 200 -s 20. Transcriptomes were extracted from species-specific gtf annotations using the gffread utility (Pertea and Pertea, 2020) using the -w output option. Human transcripts were obtained from the Gencode (Frankish et al., 2021) comprehensive gene annotation v36 (GTF), using genome assembly hg38 (Schneider et al., 2017), and the chimpanzee annotation was obtained from a recent study that produced a hierarchical alignment of primate genome assemblies (Mao et al., 2021) and annotated the assemblies using the Comparative Annotation Toolkit (Fiddes et al., 2018).

To ensure consistency of gene names across the annotations, we downloaded the set of gene aliases from the HUGO Gene Nomenclature Committee website (www.genenames.org; (Tweedie et al., 2021) and searched for gene names present in the chimpanzee but missing in the human annotation, mapped to aliases present in the human annotation. This led us to rename five genes in the non-human primate annotations (DEC1 to BHLHE40, DUSP27 to DUSP29, AC073585.2 to FAM24B,

LOR to LOXL2, and TNRC6C-AS1 to TMC6); we also renamed CCNP in the human annotation to CNTD2.

After counting transcript abundances using kallisto, we converted them to gene counts using the tximport command in the tximport R package (Soneson et al., 2015) with the options type='kallisto' and countsFromAbundance='no'. We then created one human and one chimpanzee data set in DESeq2 (Love et al., 2014) contrasting gene knockdowns with wild-type gene expression in two replicates of the same cell line in each. We extracted VST-transformed counts for plotting using the function vst with option blind=TRUE and ran the DESeq linear model fitting using the function DESeq with betaPrior=TRUE.

GO enrichment was performed on the set of genes overexpressed in cells expressing sgRNAs targeting *KAT6A* or *BRPF1*. Overexpressed genes were defined as genes with fold-change > 2 in sgRNA expressing cells. Fold-change values were averaged between cells expressing sgBRPF1 and sgKAT6A. GO enrichment analysis was performed with Enrichr (Chen et al., 2013) and significant terms from the MSigDB Hallmark gene set were most significant and relevant for chimpanzee overexpressed genes. Significant terms from WikiPathway Human and GO Molecular Function were used for human overexpressed genes, though TGF-beta signaling was also an enriched GO term in MSigDB, and genes in the cell differentiation category were partially overlapping with TGF-beta signaling genes. Morphogen activity genes were *CER1* and *NODAL*.

Gene expression changes were quantified for a set of 149 developmental marker genes with evidence from prior literature (Maguire et al., 2013). Among these genes, 21 were overexpressed by > 0.5 by $\log_2$ fold-change in either human or chimpanzee cells. 8/21 were further filtered out based on DESeq2 adjusted *P*-value. Fold-change values were averaged between cells expressing sgBRPF1 and sgKAT6A. Markers were clustered based on overexpression in both human and chimp or human alone. Markers were then clustered and colored based on their association with ectoderm, endoderm, mesoderm, or mixed lineages. Lastly, canonical pluripotency markers *OCT4*, *SOX2*, and *NANOG* were added for visual comparison, as none of these genes were significantly upregulated.

Analysis of protein-coding and gene expression changes
To obtain coding sequences for homologous transcripts from human and chimpanzee reference genomes, we downloaded human protein and transcript sequences from Gencode release 36 (Frankish et al., 2021) and chimpanzee protein and transcript sequences from the Comparative Annotation Toolkit (Fiddes et al., 2018) annotation on reference version panTro6 produced as part of a recent study (Mao et al., 2021). For each human transcript of each protein coding gene, we obtained the transcript sequence and its canonical translation, and we then extracted the corresponding chimpanzee transcript and canonical translation by matching the Ensembl transcript ID to its chimpanzee counterpart ("source transcript" field in the chimpanzee gene annotation). For both the human and chimpanzee sequence of each transcript, we then compared the translated sequence at every possible start codon and frame to the canonical amino acid sequence, determining the start codon and frame that produced the canonical amino acid sequence to be "correct" and removing bases thus found to belong to the 5' or 3' UTR (upstream of the correct start codon or downstream of the correct stop codon).

With coding sequences for homologous transcripts, we then aligned the human and chimpanzee protein sequences using the pairwise2 module from Biopython (Cock et al., 2009) with a BLOSUM62 substitution matrix. We then deleted codons in transcripts corresponding to amino acids that aligned to a gap in the other amino acid sequence. Finally, we deleted stop codons from the ends of sequences. We then wrote out each pairwise alignment to a control file for PAML (Yang, 2007) and calculated relevant statistics, including dN, dS, N, and S, using PAML's implementation of the Yang and Nielson 2000 (yn00) algorithm (Yang and Nielsen, 2000). Finally, to avoid undefined values, we set dS to 1/S where dS was zero and selected the median dN value and median dN/dS value per gene for analysis.

Distributions of dN and dN/dS were compared for the full set of genes, DepMap common essential genes, and validation screen hits by two-sided Kolmogorov-Smirnov test (ks.test in R).

Western Blot
Human (28128B) and chimpanzee (40280L) PSCs were infected with lentiviral constructs containing sgRNAs targeting ATP6AP1 or ATP6AP2. 48 hours post-infection, cells expressing sgRNA were selected for via addition of 1.5 μg/ml puromycin. Cells were then recovered in normal growth media from 4 days post-infection to 6 days post-infection. Cells were harvested at 6 days post-infection, along with separate wells of three wild-type human (H1, 21792A, 28128B) and three wild-type chimpanzee (3624K, 40280L, 8861G) cell lines. Cells from each well of a 6-well plate were lysed in ~250 μl ice-cold RIPA buffer + protease inhibitor (ThermoFisher, cat. A32965). After 30 minutes of incubation in lysis buffer at 4°C, cells were centrifuged at 16,000 x g for 5 minutes at 4°C. Supernatant was collected and snap frozen in liquid nitrogen and stored at -80°C.

Protein concentrations in each lysate were quantified using a Bradford BCA kit (ThermoFisher, cat. PI23227) Lysate was normalized to 1 μg/μl in RIPA buffer. 30 μl of lysate was added to 10 μl of NuPage Sample Buffer (4x), heated to 70°C on a PCR thermocycler, and loaded onto a Bolt 4-12% polyacrylamide gel (ThermoFisher, NW04122BOX). The gel was run for 45 minutes at 165V in MOPS buffer. Protein was then transferred onto a nitrocellulose membrane (BioRad, cat. 1704270) with a Bio-Rad Trans-Blot Turbo (BioRad, cat. 1704150). The membrane was blocked with Intercept (PBS) Blocking Buffer (LI-COR, cat. 927-90003) for 1 hour at RT. Membrane was incubated overnight at 4°C with anti-pS6 primary antibody at a 1:1,000 dilution. Membrane was washed 3x with TBST and incubated with secondary antibody at 1:15,000 dilution. Membrane was washed 3x with TBST and imaged on a LI-COR Odyssey CLX. Afterwards, antibodies were stripped from the membrane with NewBlot IR Stripping Buffer (LICOR, cat. 928-40028). Membrane was reblotted with anti-GAPDH antibody at 1:1,000 dilution and incubated overnight at 4°C. Membrane was washed 3x with TBST and incubated with secondary antibody at 1:15,000 dilution. Membrane was washed 3x with TBST and imaged on a LI-COR Odyssey CLX.

Cell cycle EdU staining
Cell cycle phase measurements were performed with the Click-iT Plus EdU Alexa Fluor 647 Flow Cytometry Assay Kit (ThermoFisher, cat. C10635). 10 μM EdU was added to cell cultures for 1 hr, after which cells were harvested with Accutase. The cell pellet was washed once with once with 500 μl PBS supplemented with 1% BSA, pelleted again, and fixed for 15 minutes at RT, protected from light. Cells were washed and permeabilized for 15 minutes at RT. EdU detection

was then accomplished via click chemistry of an Alexa Fluor 647 coupled to picolyl azide. After 1 wash, 10 µg/ml of Hoechst 33342 (ThermoFisher, cat. H3570) was added and incubated for 15 minutes. Cells were then directly analyzed by flow cytometry. Data were analyzed with custom Matlab scripts – after filtering for viable cells and doublets, G1, S, and G2/M gates were manually drawn and saved with the function impoly() for each sample. sgRNA+ populations were determined by GFP+ expression, and identical G1, S, and G2/M gates were used for sgRNA+ cells and sgRNA- cells within each sample.

Cell cycle drug treatments
For Fig. 3F, human iPSC line H28128B was used and chimpanzee iPSC line C40280L was used. Cells were infected with an sgRNA targeting FAM122A (see Table S2), with 15-30% of cells infected. No puromycin selection was performed. At day 4 post-infection, cells were Accutase passaged into StemFlex supplemented with 2 µM thiazovivin and drug, with prexasertib (Chk1i) or adavosertib (Wee1i) added at 62 nM. At day 6, cells were replated and fresh drug was added to ensure removal of dead cells. At day 8, the fraction of sgRNA+ (BFP+) surviving cells were analyzed by flow cytometry.

For Fig. 3G, human iPSC line H21792A and chimpanzee iPSC C40280L were co-cultured with a 50/50 initial seeding density. After one normal passage, cells were Accutase passaged into StemFlex supplemented with 2 µM thiazovivin and drug, with prexasertib or adavosertib added at 125 nM. 24hr after drug treatment, cells were replated and fresh drug was added to ensure removal of dead cells. 48 hr post drug treatment, the ratio of human cells (GFP+) chimpanzee cells (mCherry+) was analyzed by flow cytometry.

Neural progenitor cell differentiation
PSCs were differentiated into neural progenitor cells (NPCs) as described in (Nolbrant et al., 2017) with the following modifications. Differentiation media was made without ventral and caudalization patterning factors (sonic hedgehog agonist and GSK3i CHIR99021). PSCs were maintained on Matrigel (Corning, cat. 354230) prior to day 0 plating onto Lam-111 coated plates. Cells were seeded at 20,000 cells/cm^2, as measured by Chemometec Nucleocounter NC-202, roughly twice the published density to ensure robust survival. NPCs were evaluated for purity at days 7-11 of differentiation with antibody staining against NPC markers Pax6 and Nestin. Cells were dissociated with Accutase, pelleted and washed, then fixed and permeabilized with the BD Cytofix/Cytoperm kit (ThermoFisher, cat. BDB554714). 100 µl cells were stained with 2 µl human anti-Pax6-APC (Miltenyi, cat. 130-123-328) + 5 µl mouse anti-Nestin-PE (Biolegend, cat. 656805) and evaluated by flow cytometry. In addition, NPCs were plated on µ-Slide 4 Well chambers (Ibidi cat. 80426), stained with antibodies against Pax6 and Nestin, and visualized by fluorescence microscopy on a RPI spinning disk confocal microscope.

Orangutan CRISPRi growth comparison
CRISPRi machinery was engineered into orangutan PSCs (Field et al., 2019) at the AAVS1 locus via the three plasmid lipofection method described above (see Construction of CRISPRi cell lines). To account for mutations in the orangutan genome, the sgRNA for the Cas9 nuclease component was modified to perfectly match the orangutan AAVS1 locus. However, flanking regions were not modified. sgRNAs targeting *CDK2, CDK4, CCNE1, ATP6AP1, KAT6A,* and *UFL1* were transduced into human (28128B), chimpanzee (40280L), and orangutan PSCs via lentivirus at

MOI ~1. Cells were transduced in triplicate in 24-well plates and passaged every 2 days in ROCKi. At each passage, a portion of cells were quantified by flow cytometry on a BD LSRFortessa. The fraction of sgRNA+ expressing cells was determined based on the fraction of BFP+ cells. Measurements were collected until day 10 for *CDK2*, *CDK4*, *CCNE1*, and *ATP6AP1*. Measurements were collected until day 14 for *KAT6A* and *UFL1*. In parallel, cells transduced with sgRNAs targeting *CDK2*, *CDK4*, *CCNE1*, *ATP6AP1*, *KAT6A*, and *UFL1* and expanded into a 6 well plate. 48h post-infection, cells were expanded in 2 µg/ml puromycin and allowed to recover for 48 hours. At day 5 post-infection, sgRNA+ cells were sorted to purity based on BFP+ expression on a Sony MA900 cell sorter. RNA was extracted, cDNA was reverse transcribed, and qRT-PCR was used to quantify the degree of sgRNA-mediated depletion in biological triplicate (as described above in Quantitative RT-PCR).

Data and code availability
Raw sequencing data are deposited on GEO accession number GSE212297.
All code for the analyses performed on the CRISPRi screens is publicly available at https://github.com/tdfair.

Author contributions
R.S., T.F., J.S.W., and A.A.P. conceived the study design, executed all experiments, and wrote the manuscript. N.A.S. processed RNA-seq data and performed dN/dS calculations. R.A.S. provided the initial H1 CLYBL CRISPRi ES cell line and AAVS1 integration plasmids. B.J.P. provided high quality wildtype PSC lines and also provided extensive advice during the initial primary screens. J.S.W. and A.A.P. supervised all aspects of this work.

Declaration of interests
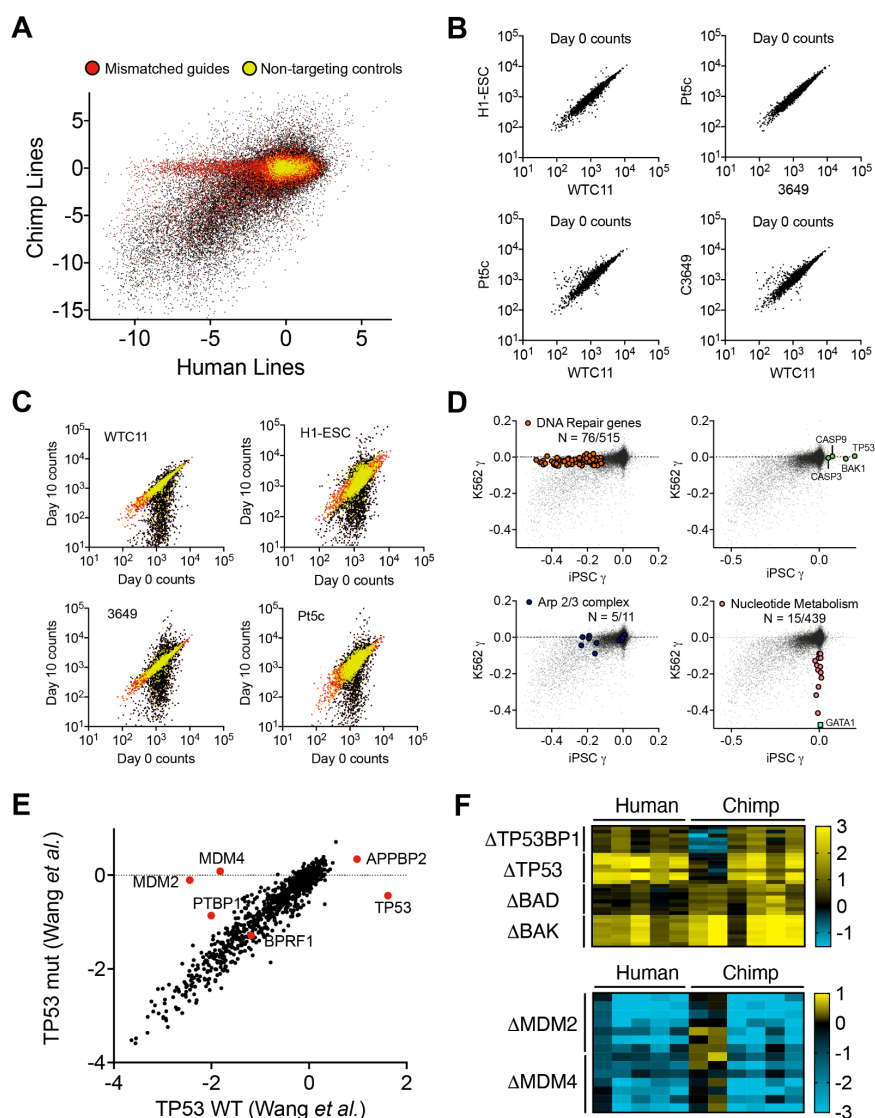The authors declare no competing interests.

Supplementary Figures

Figure S1. Genome-wide CRISPRi screens in human and chimpanzee PSCs, Related to Figure 1

(A) Log_2 fold-change of sgRNA counts from genome-wide CRISPRi screens using the hCRISPRi-2 sgRNA library, averaged across two human and two chimpanzee cell lines. sgRNAs containing mismatches to the chimpanzee genome are colored in red and non-targeting sgRNAs are colored in yellow. Thus, a substantial number of mismatched sgRNAs targeting essential genes are depleted in human PSCs but not in chimpanzee PSCs. (B) Initial distribution of sgRNAs at growth day 0 (4 days post-infection). (C) Depletion or enrichment of sgRNA counts at growth day 10 compared to growth day 0. Non-targeting sgRNAs are colored in yellow, and sgRNAs characterized as non-significant by mean-variance modeling of a negative binomial distribution are colored in red. (D) Log_2 fold-change of sgRNA counts averaged by gene (top 3) in PSC screens compared to prior screens in K562s[77]. (E) Log_2 fold-change of sgRNAs averaged by gene from screens performed in TP53 wild-type and mutant acute myeloid leukemia (AML) lines[81]. Among the differentially essential genes targeted by the CEV-v1 sgRNA library, only ~6 cause differential growth phenotypes in TP53 wild-type vs mutant cells (red) (F) Heatmap displaying log_2 fold-change of sgRNA counts across five human and six chimpanzee PSCs, with columns 1, 6, and 7

showing primary genome-wide screening data and remaining columns showing data from secondary validation screening. Columns 6 and 7 (Pt5-C and C3649) represent the two chimpanzee PSCs that exhibit TP53 mutant phenotypes.
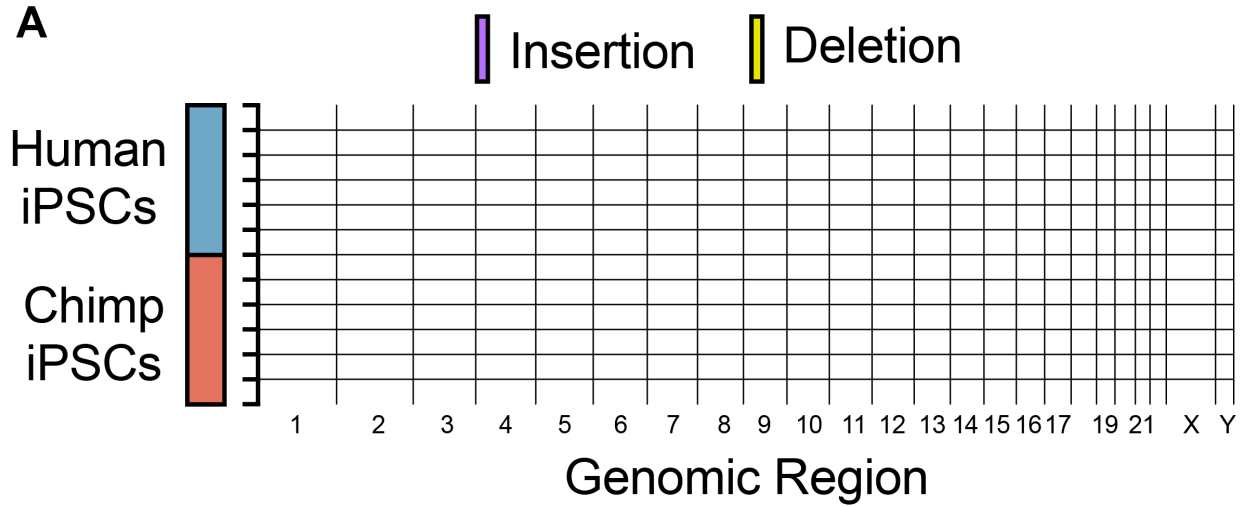
Figure S2. CEV-v1 validation screens in human and chimpanzee PSCs, Related to Figure 2. (A) CaSpER analysis of chromosomal copy number variations from bulk RNA-seq data across all newly engineered CRISPRi PSC lines as aligned to the human hg38 reference genome. For the chimpanzee genome, chromosome 2 refers to 2a and 2b.
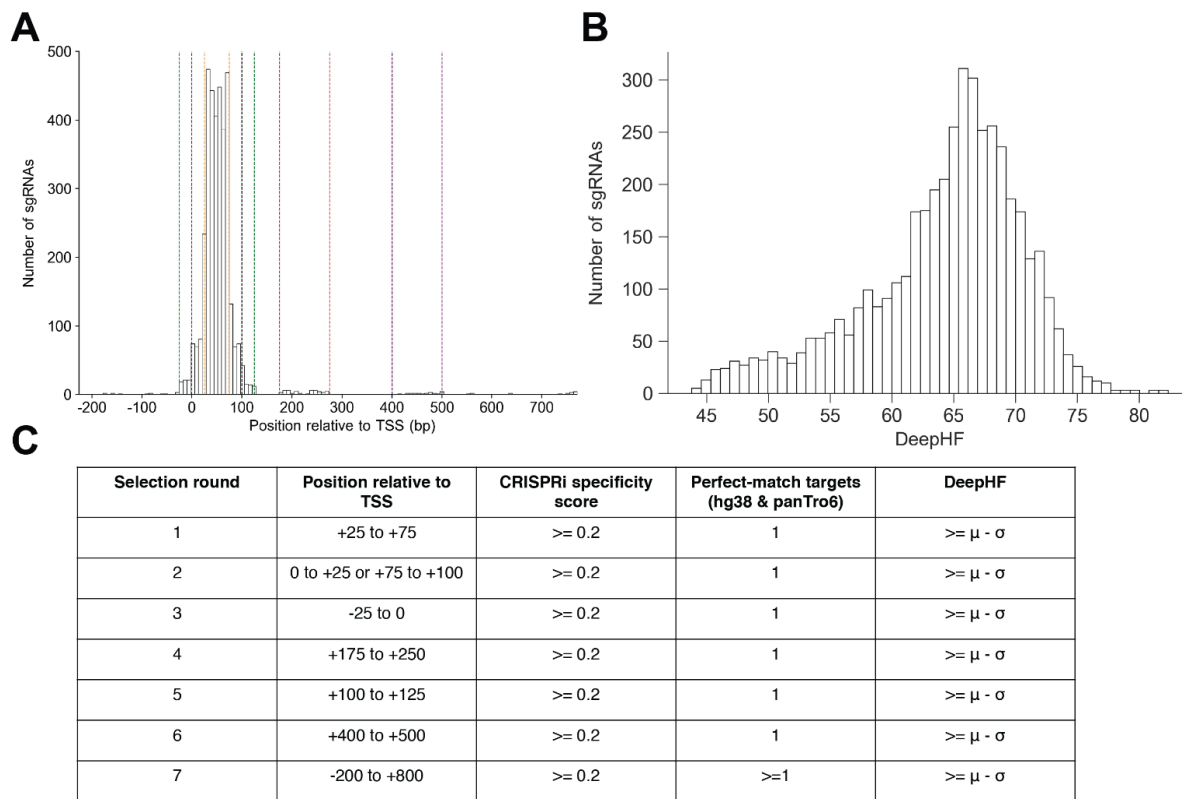
Selection round	Position relative to TSS	CRISPRi specificity score	Perfect-match targets (hg38 & panTro6)	DeepHF
1	+25 to +75	>= 0.2	1	>= μ - σ
2	0 to +25 or +75 to +100	>= 0.2	1	>= μ - σ
3	-25 to 0	>= 0.2	1	>= μ - σ
4	+175 to +250	>= 0.2	1	>= μ - σ
5	+100 to +125	>= 0.2	1	>= μ - σ
6	+400 to +500	>= 0.2	1	>= μ - σ
7	-200 to +800	>= 0.2	>=1	>= μ - σ

Figure S3. Design of CEV-v1 sgRNA library, Related to Figure 2.
(**A**) Distribution of positions relative to the FANTOM-annotated TSS for sgRNAs in CEV-v1. Vertical colored lines indicate the selection round in which sgRNAs were chosen. (**B**) Distribution of DeepHF on-target predictions for sgRNAs in CEV-v1. (**C**) Selection criteria for CEV-v1 sgRNA library.
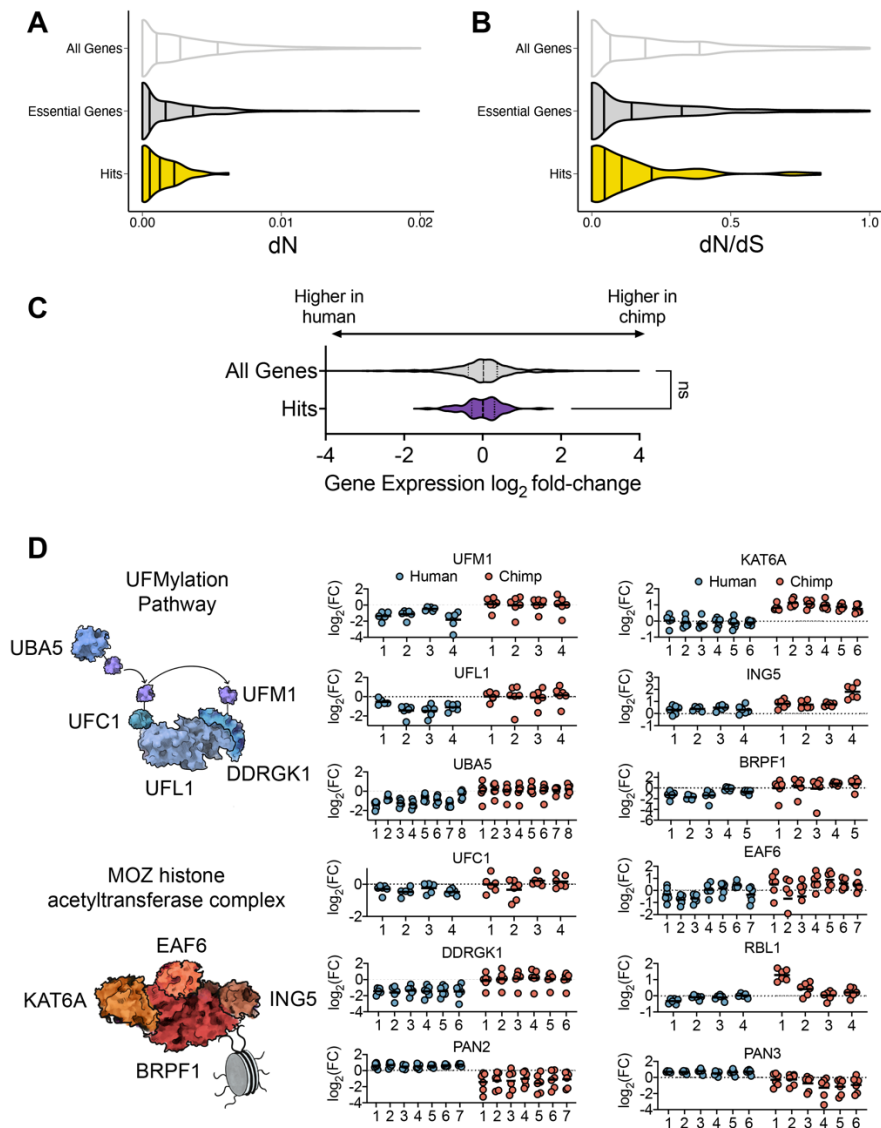
Figure S4. Species-specific genetic dependencies interact in biological processes and complexes, Related to Figure 3.

(A) dN and dN/dS values for 75 validated differential-essentiality genes from this study compared to all genes or essential genes. (C) Comparative gene expression levels between human and chimpanzee PSCs for 75 validated differential-essentiality genes from this study vs. all genes expressed in PSCs. (D) sgRNA depletion or enrichment for all active sgRNAs targeting members of the UFMylation pathway, MOZ histone acetylation complex, RBL1, and the Pan2/3 complex. Each circle represents the sgRNA fold-change for one sgRNA in one human (blue) or chimpanzee (red) individual. Each stripplot contains a variable number of columns, corresponding to the number of significant sgRNAs targeting each gene. Genes with only one significant sgRNA (*ING5* and *RBL1*) are scored as less significant compared to genes with multiple significant sgRNAs and require validation of on-target effects.
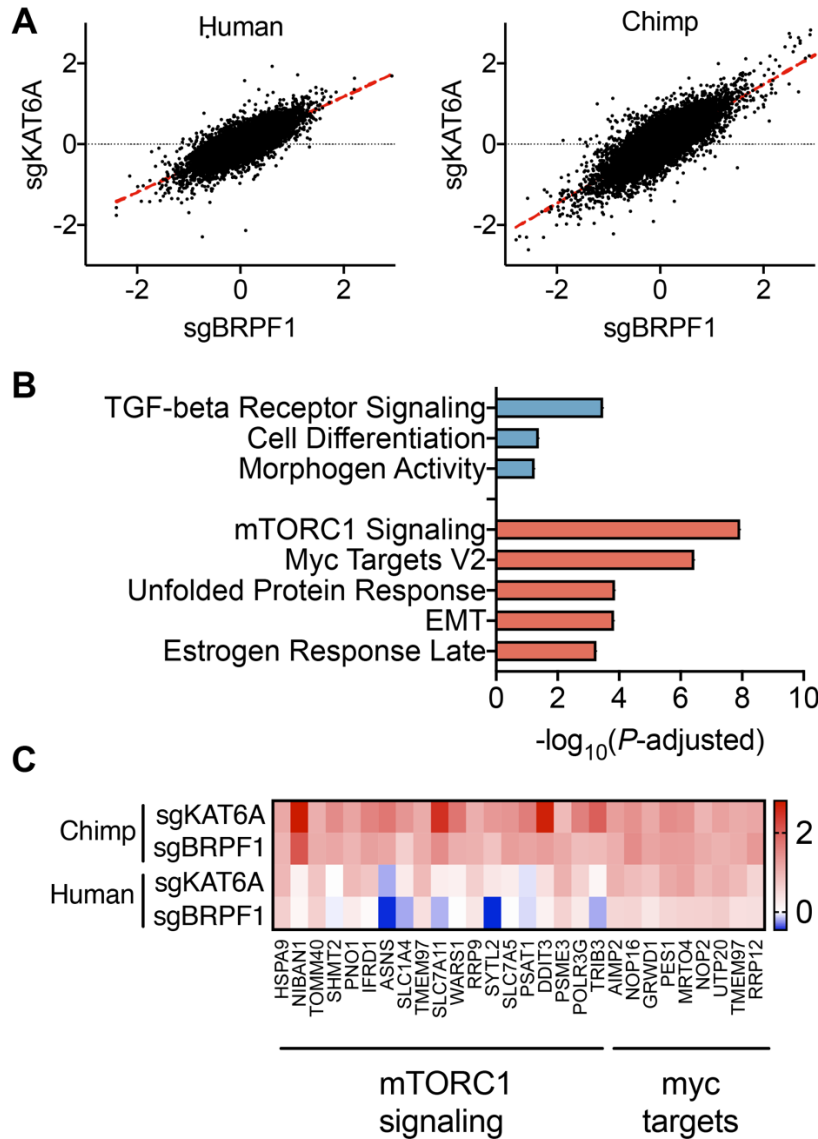
Figure S5. GO ontology enrichment for overexpressed genes in human and chimpanzee cells expressing sgKAT6A or sgBRPF1, Related to Figure 3.

(A) $-\log_{10}$ adjusted P-values for overexpressed genes in human (blue) and chimpanzee (red) cells expressing sgBRPF1 or sgKAT6A. Overexpressed genes were defined as genes with fold-change > 2 in sgRNA expressing cells. Fold-change values were averaged between cells expressing sgBRPF1 and sgKAT6A. (B) Heatmap of RNA-seq expression data for human and chimpanzee cells depleted for KAT6A or BRPF1.
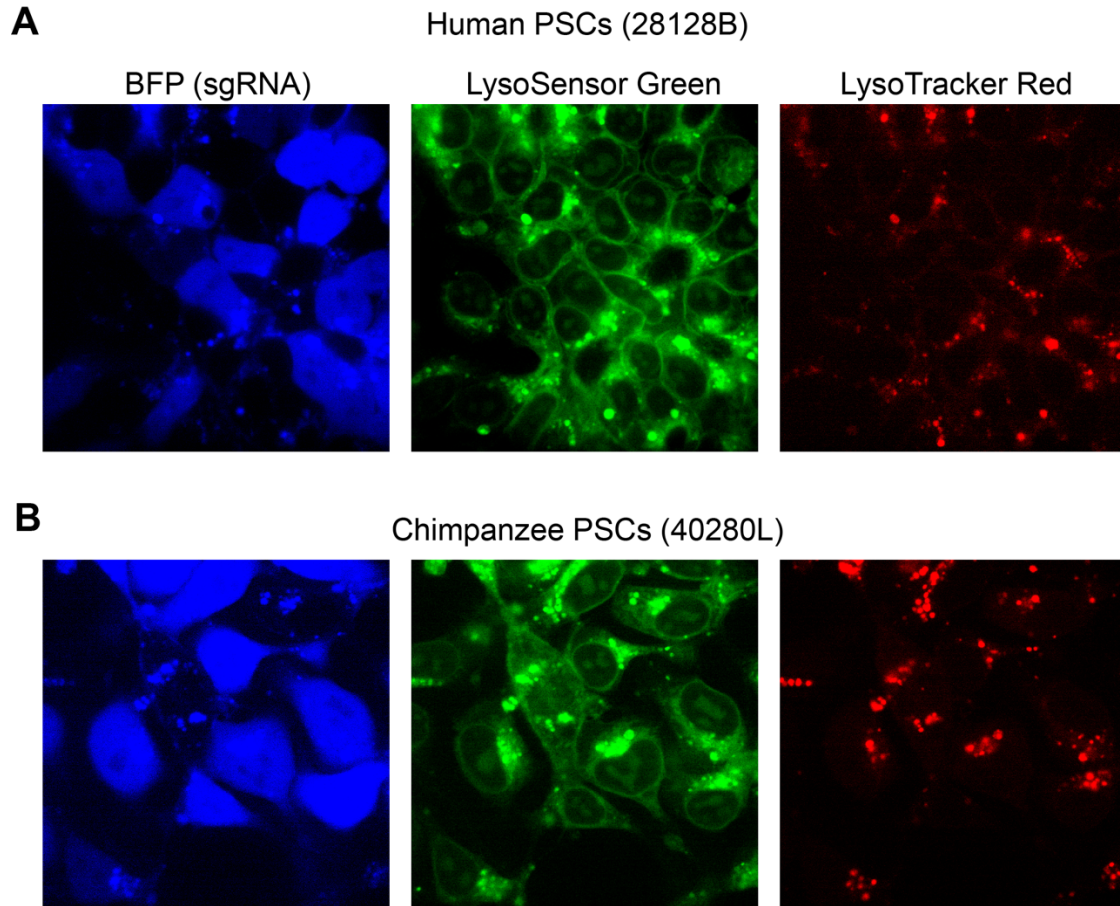
A   Human PSCs (28128B)

BFP (sgRNA)   LysoSensor Green   LysoTracker Red

B   Chimpanzee PSCs (40280L)

Figure S6. LysoTracker Red and LysoSensor green in *ATP6AP1* depleted cells, Related to Figure 3.
(A) Co-culture of human PSCs (28128B) with wild-type cells (BFP-) and cells expressing sgATP6AP1 (BFP+) stained with LysoSensor Green and LysoTracker Red. (B) Co-culture of chimpanzee PSCs (40280L) with wild-type cells (BFP-) and cells expressing sgATP6AP1 (BFP+) stained with LysoSensor Green and LysoTracker Red.
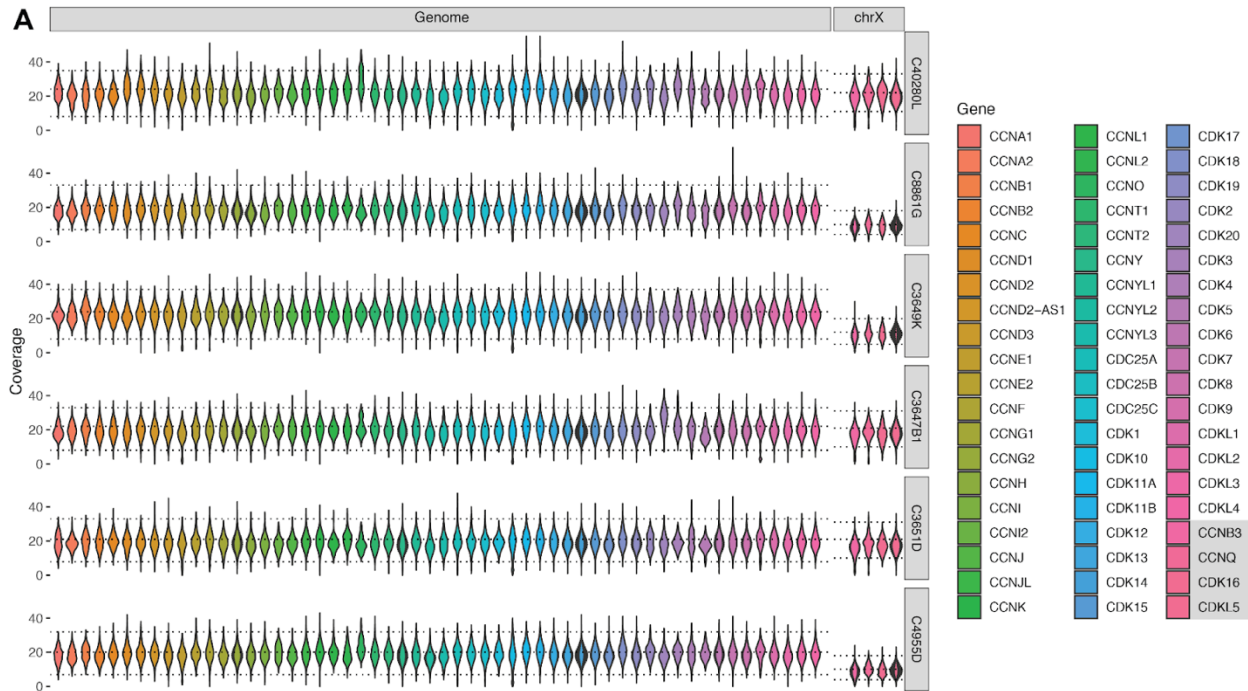
Figure S7. Analysis of whole-genome shotgun sequencing coverage at cyclin-CDK genes in chimpanzee PSCs, Related to Figure 4.

(A) Whole-genome shotgun sequence coverage at all genes in the HUGO Gene Nomenclature Committee gene groups cyclins, cyclin dependent kinases, and class III Cys-based CDC25 phosphatases (https://www.genenames.org/). Each violin represents the coverage at each base across the entire body for each gene. The horizontal lines correspond to the 5th, 50th, and 95th percentiles of baseline coverage across the entire genome ("Genome" panel) or the X chromosome ("chrX" panel). Four genes in these sets located on chromosome X (CDKL5, CDK16, CCNB3, CCNQ) are shown separately to account for different baseline coverage; these gene names are outlined in a gray box in the legend. The top three rows correspond to chimpanzee PSCs from individuals used in the present study (C40280L, C8861G, C3649K), while the bottom three rows correspond to similarly reprogrammed chimpanzee individuals.
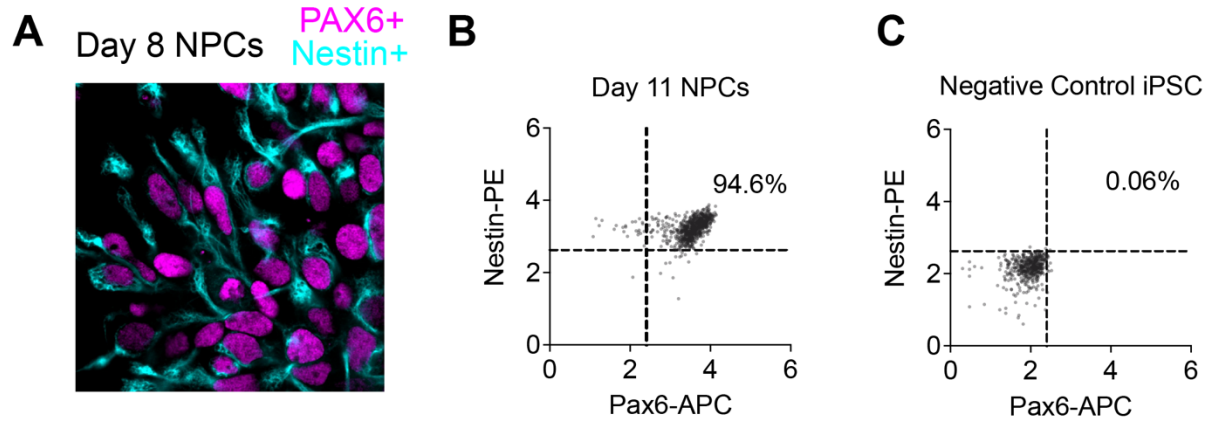
Figure S8. Derivation of human and chimpanzee NPCs, Related to Figure 5.
(A) Chimpanzee neural progenitor cells (C40280L) stained for Pax6 and Nestin, visualized by confocal microscopy. (B) Chimpanzee neural progenitor cells (C40280L) stained for Pax6 and Nestin, quantified by flow cytometry. (C) Negative control PSCs stained for Pax6 and Nestin, quantified by flow cytometry.
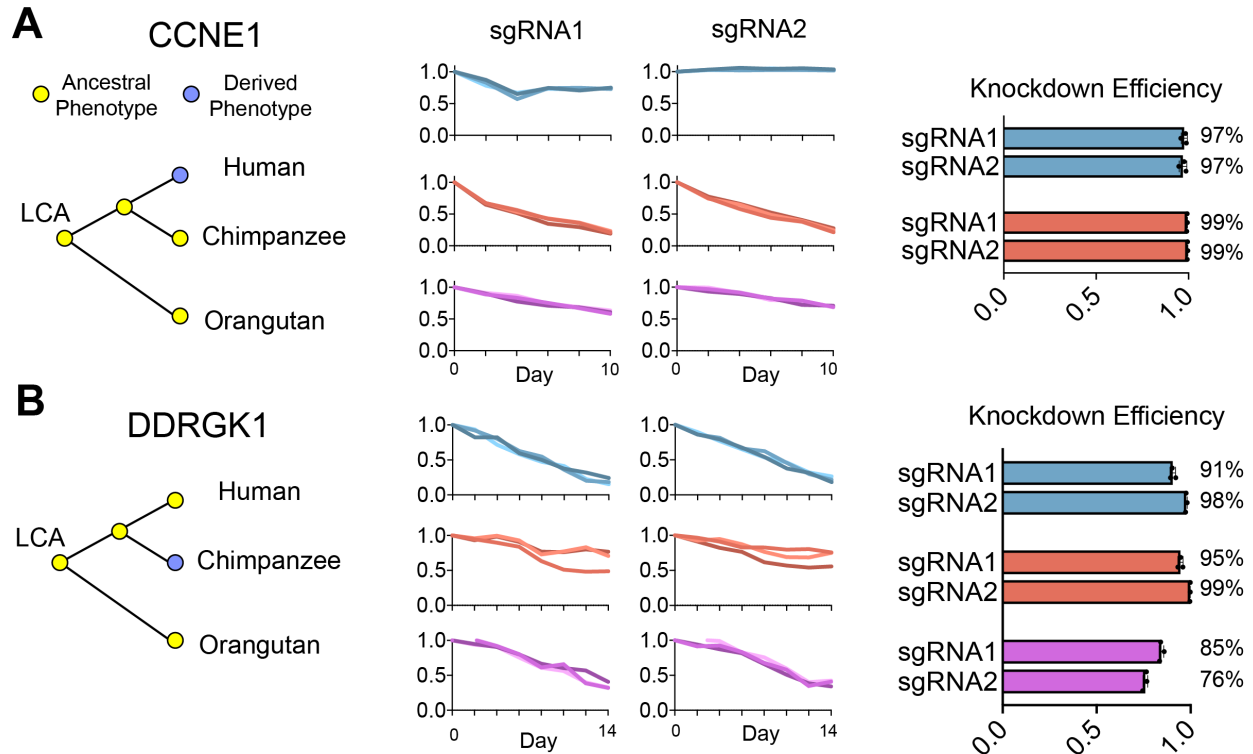
Figure S9. Tri-species comparison of human, chimpanzee, and orangutan PSCs expressing sgRNAs targeting *CCNE1* and *DDRGK1*, Related to Figure 6.
(A-B) Change in the relative fraction of CCNE1 (A) and DDRGK1 (B) sgRNA containing cells over time in human, chimpanzee, and orangutan PSCs. qRT-PCR measurements of sgRNA knockdown efficiency for each sgRNA.

Tables (Separate file)

Table S1. Cellular metadata for primary CRISPRi screen and CEV-v1 screens

Table S3. sgRNA counts from hCRISPRi-v2 genome-wide screens

Table S4. hCRISPRi-v2 sgRNA library

Table S5. sgRNA counts from CEV-v1 validation screens

Table S6. qRT-PCR primers and individual sgRNA primers

Table S7. Transcriptional responses to *BRPF1* and *KAT6A* repression in human and chimpanzee PSCs